heritage

MDPI

Article

Coloring of Spun Glass Figurines Attributed to Nevers—A Huge Variety of Composition Imposed by the Preparation Process

Philippe Colomban [1,*], Gulsu Simsek-Franci [2] and Marie-Lys Chevalier [3]

[1] Laboratoire 'De la Molécule au Nano-Objet: Réactivité, Interaction et Spectroscopies, (MONARIS UMR8233), Sorbonne Université, CNRS, Campus P.-et-M. Curie, 4 Place Jussieu, 75005 Paris, France
[2] Department of Metallurgical and Materials Engineering, Faculty of Chemical and Metallurgical Engineering, Yildiz Technical University, Davutpasa Mah. Davutpasa Caddesi, 34220 Istanbul, Türkiye; gulsu.simsek@yildiz.edu.tr
[3] Musée de la Faïence et des Beaux-Arts-'Frédéric Blandin', 16 rue Saint-Genest, 58000 Nevers, France
* Correspondence: philippe.colomban@sorbonne-universite.fr

Abstract

For the first time, twenty spun polychrome glass figurines (considered as tangible cultural heritage objects) stylistically assigned to workshops of the city of Nevers from the 17th to 19th centuries have been analyzed at the Musée de la Faïence et des Beaux-Arts of Nevers using non-invasive XRF and Raman spectroscopy. The results are compared with those previously obtained for figurines assigned to the Perrot's Orléans workshop. A wide variety of glass compositions is observed, ranging from lead-free to lead-rich compositions, which are attributed to the preparation technique that involves mixing glass stems of different origins during the creation of the figurine. White opacification is achieved with $Ca_2Sb_2O_7$. The cobalt source is consistently arsenic-rich, but its composition becomes more complex during the 18th century, indicating the use of different cobalt sources. A variety of lead-tin and Naples yellow pigments are identified. Metal nanoparticles are used for pink, ruby, and carnation colors. The detection of associated arsenic and/or tin supports the identification of the use of gold nanoparticles. Cassiterite and arsenates of lead/calcium/potassium are also detected in a few figurines, probably from a different workshop. This latter opacifier, being more frequent in previously studied artifacts assigned to Orléans, suggests that the assignment to Nevers could be questioned. Aventurine glass is present in two objects.

Keywords: spun glass; figurine; Nevers; pXRF; Raman spectroscopy; 17th century; 18th century; 19th century; cobalt; composition; Naples yellow; white; blue; aventurine

Check for updates

Academic Editor: Artemios Oikonomou

Received: 27 April 2026
Revised: 26 May 2026
Accepted: 10 June 2026
Published: 12 June 2026

Copyright: © 2026 by the authors. Licensee MDPI, Basel, Switzerland. This article is an open access article distributed under the terms and conditions of the Creative Commons Attribution (CC BY) license.

1. Introduction

From the 17th century, or earlier according to the texts, probably since the reign of Henry IV (1589–1610), the production of spun glass figurines in the city of Nevers is attested in collections. Nevers, capital of the Duchy of Nevers, was a possession of the princes of Gonzaga since Louis Gonzaga (Ludovico Gonzaga in Italian, 1539–1595), prince of Mantua, who was sent at a very young age to the court of France, raised with the children of the royal family of Valois, and in 1565 married Henriette de Clèves, heiress to the Duchy of Nevers (center of France) and the County of Rethel (north-east of France).

The first glass workshops to manufacture advanced glass objects (glassware, bottles, etc.) in Nevers are considered to date from 1582, following the arrival of Italian glassmakers from the region of the Duchy of Mantua, well after the workshops of Avignon (1443), seventy years after those of Lyon (1511), and a few years after Antwerp (1541), but

before those of Mâcon (1583), Chalon (1583), Nantes (1584), Melun (1597), Rouen (1598), and Paris (1606) [1]. Before this, glass workshops were associated with the construction of churches, producing stained glass or standard windows.

To our knowledge, the oldest preserved figurines attributed to Nevers workshops date from the 17th century, that is to say from the time of Charles I Gonzaga, son of Louis Gonzaga, Duke of Nevers, Mantua, and Montferrat (Italy), Prince of Arches (now Charleville, France). In 1659, the duchy was sold to Cardinal Mazarin, prime minister of King Louis XIII, and his nephew Philippe Julien Mazarini-Mancini inherited it two years later. The duchy remained in the possession of the Mancini, Dukes of Nevers and Grandees of Spain, until the French Revolution. The ducal court therefore remained linked to European royal courts for several centuries, supporting high-quality craftwork.

We present here the first comprehensive study, by X-ray fluorescence spectroscopy and inelastic micro-spectroscopy of light (Raman scattering), of the coloring agents (and opacifiers) of 20 objects stylistically attributed to the 17th, 18th, and 19th centuries, belonging to the collection of the Musée de la Faïence et des Beaux-Arts-Frédéric Blandin in the city of Nevers.

Very few teams have, to date, conducted on-site analyses of exceptional glass objects, whether through optical spectroscopy or elemental analysis. The rarity and fragility of these objects prohibit any sampling or physical contact and make their transport to a laboratory extremely expensive. Consequently, studies on spun glass figurines remain very limited. According to Lanmon & Whitehouse [2], the production of spun polychrome figurines developed in the 16th century in Venice before spreading to France, Germany, and England. The starting material consists of solid glass rods, worked '*a lume di candela*', that is to say with a flame, a technique that can be carried out at home or in a small workshop. The glass therefore had to be highly fusible (called "*rocaille*" glass, that is to say rich in lead and other fluxes) in order to be shaped in a pasty/viscous state on a skeleton made of "iron" wire [3–7]. The figurines can be combined in groups within a glass or wooden setting to form a diorama [3]. Like all glass objects, signatures are exceptional, which complicates dating. In addition, the claimed origin of objects acquired on the art market at different periods may be questioned.

Ten figurines attributed to the workshop of Bernard Perrot, glassmaker to King Louis XIV, analyzed by Raman scattering in 2020 at the Orléans city museum [8], will be used for comparison. The previous study was very limited in scope: a polychrome figurine and a few fragments of white and green glass from figurines attributed to the city of Nevers were studied by sampling to determine their microstructure and composition [9–11]. Knowledge of these productions therefore remains very basic, and the new possibilities offered by mobile Raman and X-ray fluorescence instrumentation, recently demonstrated in the semi-quantitative study of European and Chinese porcelain enamels [12–14], can provide new information on the manufacturing, coloring, and opacification techniques of these glass objects.

2. Materials and Methods

2.1. Portable X-Ray Fluorescence Spectroscopy (pXRF)

The procedure has been described in detail in previous articles [12–14]. X-ray fluorescence analysis was performed on site (Figure 1) using a portable instrument (Elio-Bruker, Berlin, Germany). The set-up included a miniature X-ray tube system with a rhodium anode, a ~1 mm^2 collimator, and a large-area Silicon Drift Detector with an energy resolution of <140 eV for Mn Kα, and a detection energy range from 1.3 keV (in air) to 43 keV. The working distance between the instrument front and the analyzed spot is about 1 cm, which permits the selection of colored areas located on relatively flat or convex zones. Depending

on the object, the measurement was performed by positioning the instrument from the top or from the lateral side. Perfect perpendicularity to the measured area was sought.



Figure 1. View of the mobile devices: on the left, the Raman spectrometer (placed on its transport case) being connected by optical fiber to the laser and to the measuring head placed on an X–Y–Z micrometric displacement stage in front of the object, the entire setup being isolated from ambient light by a black fabric. On the right, the XRF spectrometer mounted on a photographic tripod via a motorized X-Y stage, the movement perpendicular to the object (Z-axis) being manual using a micrometric device. The detailed views show the absence of contact with the object (top: Raman analysis; bottom: XRF analysis).

Measurements were carried out in point mode with an acquisition time of 180 s for white, yellow, and black colors, and 360 s for blue area (because the cobalt Kα and iron Kβ signals overlap, the noise must be minimized to allow deconvolution of the components), using a tube voltage of 50 kV and a current of 80 μA. The current was limited to 50 μA for the metal wire. The analysis depth, defined as the thickness of the top layer from which 90% of the fluorescence originates [15], was determined using the Beer–Lambert law to be approximately 6 μm at Si Kα, 170 μm at Cu Kα, 300 μm at Au and Pb Lα, and 3 mm at Sn Kα.

The accuracy of the instrument is controlled by the measurement of reference standards. The data fitting procedure using Artax 7.4.0.0 (Bruker, AXS GmbH, Berlin, Germany) software has been reported in previous papers [12–14]. To address this, we compared the areas of characteristic peaks, as done in previous studies. The net area under the peak at the characteristic energy of each selected element in the periodic table was calculated, and the counts of the major, minor, and trace elements were determined for the colored areas. Before plotting the diagrams, the net areas for each element were normalized by the number of XRF photons derived from the elastic peak of the rhodium X-ray tube. The normalized data were then plotted in ternary scatter plots for interpretation and discussion using Statistica® 13.5.0.17 developed by TIBCO Software (Palo Alto, CA, USA). Since the 1980s, chemometrics, also known in the archaeometry literature as multivariate statistical analysis [16–29], has been particularly well-suited to the analysis of complex and high-dimensional data, such as semi-quantitative pXRF analyses, enabling the extraction of meaningful patterns and features from intricate datasets. Today, even social scientists without a strong background in mathematics or statistics can use software such as Statistica® 14.1.0, analytical modules developed by the Python Software (3.14.5) Foun-

dation (Wilmington, DE, USA), Minitab® 22 (State College, Pennsylvania, PA, USA), and SPSS® v30 developed by IBM (Armonk, NY, USA) to compare datasets and make various technological interpretations. For clustering/similarity analysis (dendrograms), the dataset was first explored using the Pandas library 3.0.x (NumFOCUS, Inc., Austin, TX, USA). Agglomerative clustering using the sklearn.cluster® 1.9.0 module was then performed. To visualize and illustrate the composition of each cluster, dendrograms were generated, displaying the points in each cluster and their relative distances. Ward's method was selected and implemented as the linkage method, using the scipy.cluster.hierarchy® 1.17.1 module (open source, GitHub, Inc., San Francisco, CA, USA) for visual representation and matplotlib® 3.10.9 for plotting. The code was developed and executed in a Jupyter Lab® environment, version 4.1.6 (Jupyter.org, Santa Teresa, NM, USA).

2.2. Raman Micro-Spectroscopy

The complete description of the procedure used with the HE532 Raman spectrometer (HORIBA Jobin-Yvon, Palaiseau, France), equipped with a 300 mW 532 nm Ventus laser (Laser Quantum, Fremont, CA, USA), a Peltier cooled charge-coupled device (CCD) detector (HORIBA Jobin-Yvon, Palaiseau, France), and a remote SuperHead® (HORIBA Jobin-Yvon, Palaiseau, France) connected by optical fibers to the laser and the spectrometer, has already been given in previous studies [12–14]. A long working distance (LWD) 200× microscope objective (Mitutoyo Corp., Tokyo, Japan) was used (Figure 1). The analyzed spot is about 1×1 µm^2; the in-depth penetration is similar for light-colored glaze but strongly reduced for dark-colored areas. A 50–3200 cm^{-1} spectral window was recorded. The full counting time ranged from a few minutes to ten minutes; at least three accumulations were required to suppress cosmic ray signals. The limited resolution of the instrument led to an uncertainty of ±2 to 3 cm^{-1} in the wavenumbers.

2.3. Objects

Table 1 lists the 19 figurines and a representation of Christ on the cross, in the order of their attributed dates (along the first column and then the second one): ten figurines from the 17th century (mythological allegories and religious characters), fives from the 18th century, and four from the beginning of the 19th century, the latter depicting King Louis XVIII dressed in a long coat embroidered with fleurs-de-lis and covered with an ermine cape, the Duchess of Angoulême (Marie-Thérèse Charlotte de France, nicknamed Madame Royale), the Duke of Berry, and the Duke of Angoulême (Louis-Antoine d'Artois, who became Louis-Antoine de France). The colors of the areas analyzed by Raman and XRF are indicated.

Table 1. Spun glass figurines attributed to the Nevers workshops (n.a.: not analyzed).

View	Inventory Number, Description (H/D: cm) Period	Analyzed Color		View	Inventory Number, Description (H/D: cm) Period	Analyzed Color	
		Raman	XRF			Raman	XRF
	OAP 798 Pilgrim of St-Jacques (15) 17th c.	White (carnation) Blue Yellow Black	White (carnation) Blue Yellow Black		NOA 969.2.4.3 Shepherd (7.5) 4th quarter of the 18th c.	White Blue Yellow Black	White Blue Yellow Black Metal

Table 1. *Cont.*

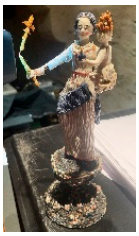
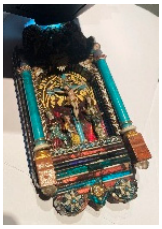
View	Inventory Number, Description (H/D: cm) Period	Analyzed Color		View	Inventory Number, Description (H/D: cm) Period	Analyzed Color	
		Raman	XRF			Raman	XRF
	OAP 769 Lady (16) 2nd quarter of the 17th c.	Blue Yellow Brown	White (carnation) Blue Yellow Brown		NOA 310 Virgin with child (20.9) 4th quarter of the 18th c.	White Blue Pink	White Blue Pink Green Glass Metal
	OAP 770 The real drinker (12.5) 2nd half of the 17th c.	White Blue Yellow Black Glass	White Blue Yellow Black Glass		NOA 255 Gosling merchant (10.3) 4th quarter of the 18th c.	White Black Pink Yellow	White Blue (pale) Blue Turquoise Pink Yellow Black
	OAP 777 Pomone (16) 3rd quarter of the 17th c.	White Blue Black Metal	White Blue Pink Black		OAP 756 St-Pierre (18) 4th quarter of the 18th c.	White Blue (dark) Blue (pale) Pink Yellow	White Blue (dark) Yellow Aventurine Black Green Red
	NOA 2006.0.64 St-Jerome (11.2) 3th quarter of the 17th c. (restauration)	White Pink Yellow	White Pink Black Brown Glass		OAP 784 Virgin with child (13) 4th quarter of the 18th c.	White Blue Blue (dark) Pink Yellow	White Blue Blue (dark) Pink Yellow
	NOA 961.4.6 The good Shepherd (7.1) 4th quarter of the 17th c.	White Blue Brown Red	White Blue Brown Red		NOA 2016.2.1 Louis XVIII (10) circa 1815 (the legs have been restored)	White	White Blue Blue (dark) Pink Yellow Orange Black Brown

Table 1. *Cont.*

View	Inventory Number, Description (H/D: cm) Period	Analyzed Color		View	Inventory Number, Description (H/D: cm) Period	Analyzed Color	
		Raman	XRF			Raman	XRF
	NOA 213.1 The Spring (allegory) (15.2) 4th quarter of the 17th c.	n.a.	White Blue Pink Red		NOA 2016.2.2 Duc de Berri (10) circa 1815	n.a.	White (carnation) Blue Yellow Black
	NOA 213.2 The Summer (allegory) (15.5) 4th quarter of the 17th c.	n.a.	White Pink Yellow Green Brown Red Glass		NOA 2016.2.3 Duchess d'Angouleme	n.a.	White Pink Black Brown Green Glass
	NOA 213.3 The Autumn (allegory) (15.3) 4th quarter of the 17th c.	White Yellow-green Black Glass	White Carnation Yellow Green Black Glass		NOA 2016.2.4 Duc Angouleme (10) circa 1815	n.a.	White Blue Yellow Black
	NOA 213.4 The Winter (allegory) (15.3) 4th quarter of the 17th c.	White Blue Black Brown	White Blue Pink Yellow- Aventurine Black Glass		OAP 765 Crucifix (22) 17th (figurines) and 18th (miniature Altar piece)	n.a.	White Blue (gem) Turquoise Gold

The four allegories of the seasons (Figure 2) are a good example of the quality of 17th century spun glass. The Pilgrim of St-Jacques, whose face was considered by Jean Loynel d'Estrie, the collector behind part of the Nevers Museum collection, to represent Louis Gonzaga, is particularly representative of the quality that certain spun glass figurines can achieve despite their small size. The broken arm of the allegory of summer reveals the metal wire used as a support during the creation of the softened glass figure.



Figure 2. Detail of the allegories of the seasons (from left to right, top to bottom: spring ((**a**), NOA 213.1), summer ((**b**), NOA 213.2), autumn ((**c**), NOA 213.3), and winter ((**d**), NOA 213.4)), and views of the faces of the Pilgrim of St-Jacques ((**e**), OAP 798) and the Duke of Berry ((**f**), NOA 216.2.2); see Table 1 for more characteristics.

3. Results

All the collected spectra and Tables of data are provided in the Supplementary Materials for each object.

3.1. Metal Frame

Figure 3 shows the spectrum of a portion of the metal rod revealed by the loss of the arm. The dominant signal is that of iron; other contributions come from the blue glass in the background. In agreement with the literature [3], the metallic element is iron; however, it is not possible to determine whether the rod is soft iron or steel, as carbon detection is not possible by XRF.

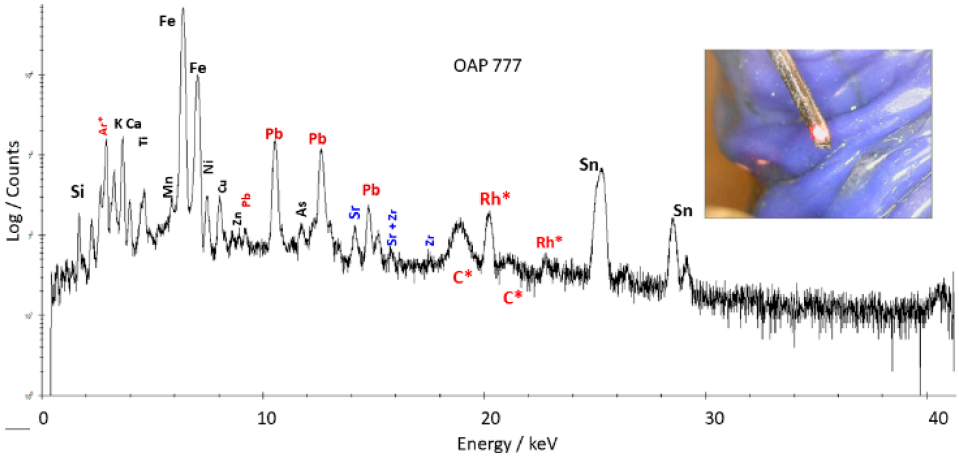


Figure 3. XRF spectrum of the metal structural frame of the OAP 777 figurine. Signals arising from the rhodium source, argon in air, and Compton scattering are highlighted in red and marked with an asterisk.

3.2. Flux

Figure 4 illustrates the diversity of vitreous compositions observed, including within the same object, as exemplified by NOA 961.4.6, 'The good Shepherd' figurine, which shows the simultaneous use of lead-rich (blue) and lead-poor (red) glass. Some glass parts may even be virtually lead-free.

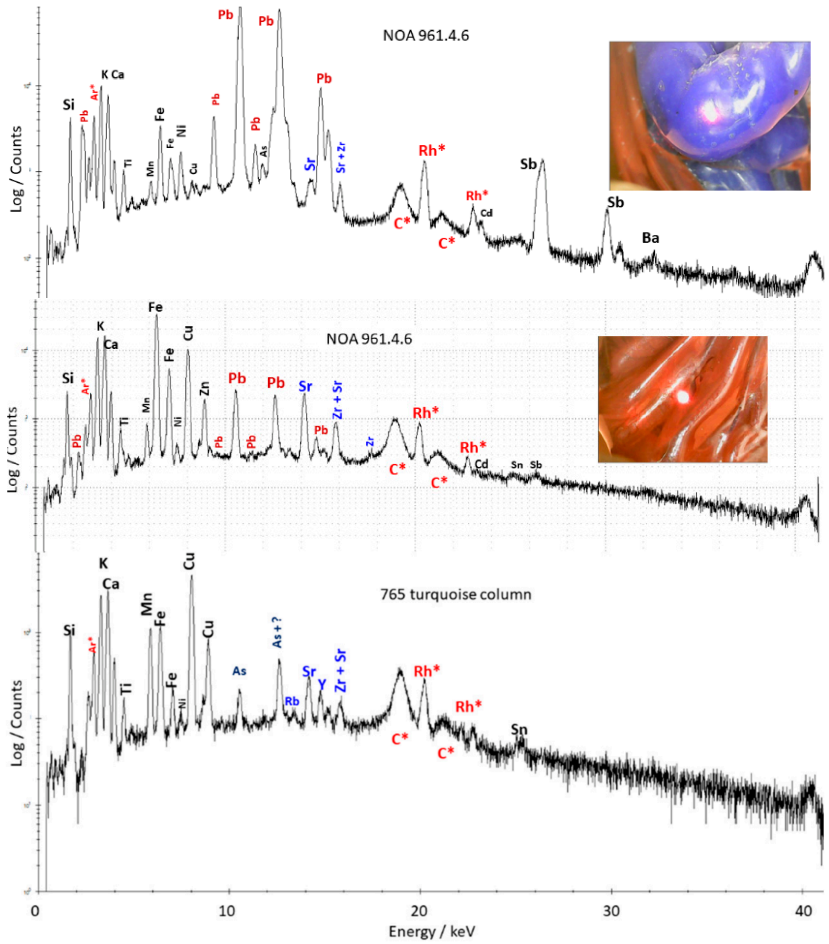


Figure 4. Comparison of the XRF spectra obtained on the red and blue glass of 'The good Shepherd' (top, inv. NOA 961.4.6, 4th quarter of the 17th c.) and on the turquoise pillar of the Christus on the cross (inv. OAP 765).

The Si-Pb-K and Pb-K-Ca ternary diagrams (Figure 5), constructed from the corresponding elemental peak areas, show that all data points lie along a line starting from a K/Si signal ratio close to 0.19. The very different Si-rich composition corresponds to the pale blue quartz bead above the columns of OAP 765 artifact. Due to the very strong XRF signal of lead and the relatively strong potassium signal compared to silicon, partly affected by absorption, the data point corresponding to the blue gem (OAP 765) is not located very close to the Si apex. As the diagrams are based on peak areas, the contributions of elements producing intrinsically intense peaks are emphasized: the visualization is thus different from that obtained using compositions.

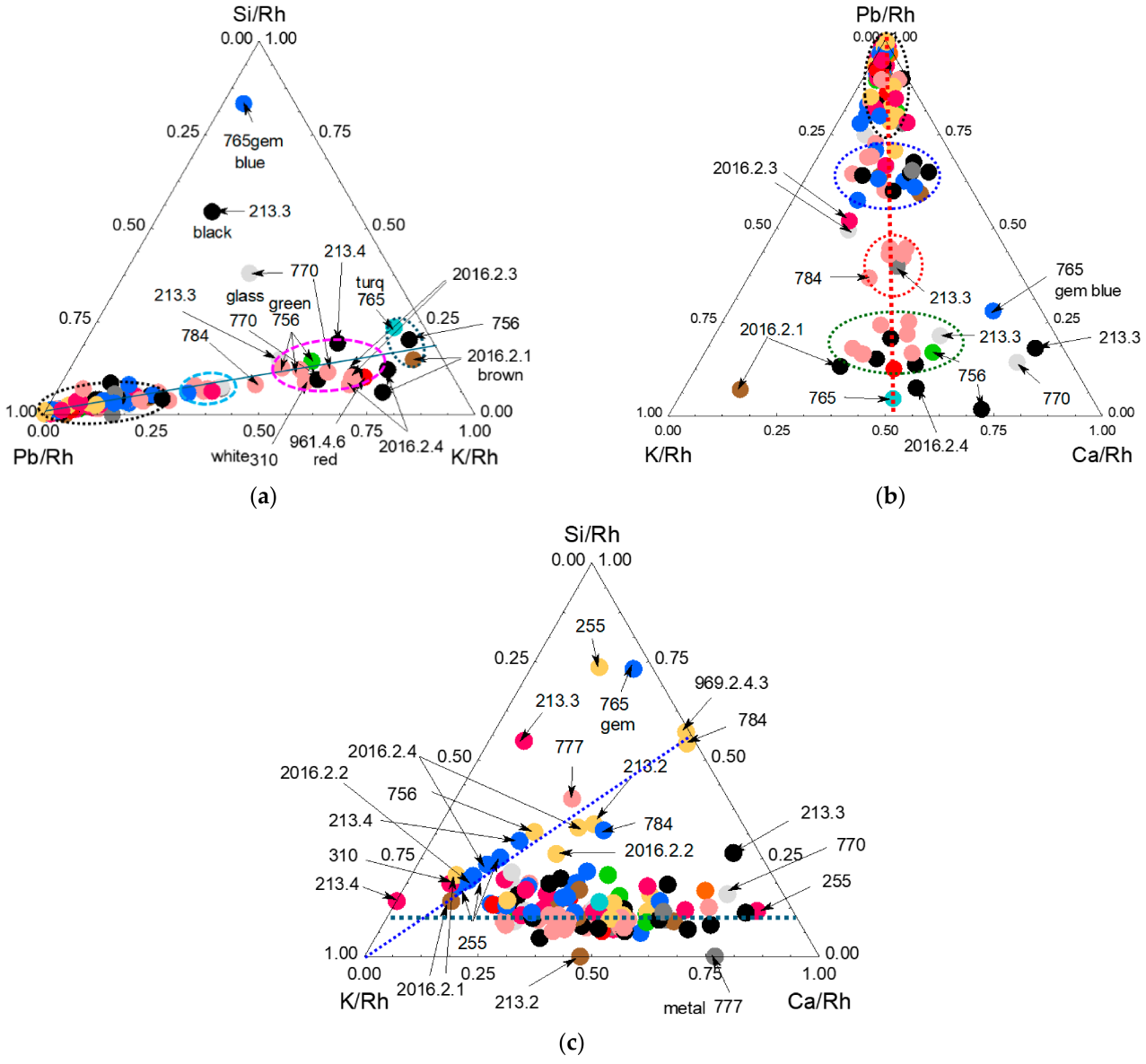


Figure 5. Si-Pb-K (**a**), Pb-K-Ca (**b**), and Si-K-Ca (**c**) ternary diagrams constructed from the corresponding element peak areas normalized by Rh. Inventory numbers are given (see Table 1, letters have been omitted in the diagrams). Color of the dot corresponds to the color of the glass (Dashed and doted lines are visual guides).

Taking signal efficiency into account, four groups can be identified: one essentially free of lead (ppm level), one with minor lead impurities (% level), one with a low lead content, and another with significant to high lead content. Only two measurements deviate from the linear trend, which may reflect glass inhomogeneity.

The Pb-K-Ca diagram shows that the K/Ca ratio remains constant. This suggests that the figurine maker used two types of glass tray: a lead-rich glass and a K-Ca glass (note that sodium, lithium, and boron cannot be detected with pXRF).

The Raman spectra (Figure 6) confirm the variability in glass types. Some correspond to mixed soda-potash-lime compositions, characterized by a main broad SiO_4 stretching band around 1090 cm^{-1}, with minor components at 940 and 995 cm^{-1} which represent a mixed potash-soda-lime glassy silicate [30]). Others are richer in lead, which enhances the component near 980 cm^{-1}, becoming dominant in yellow-colored glasses (Figure 6). Compositional variation is also reflected in the peak area ratio between the bending modes and stretching modes of the SiO_4 tetrahedra, which changes with composition [30]. However, due to the background associated with the use of optical fibers, this ratio is difficult to determine precisely using a mobile instrument, making it challenging to extract the melting temperature of glassy silicate from its Raman signature. In some instances, such as the brown glass shown in Figure 6, the spectrum is largely dominated by background noise. The weak signal measured for the brown glass also excludes the use of hematite as a coloring agent.

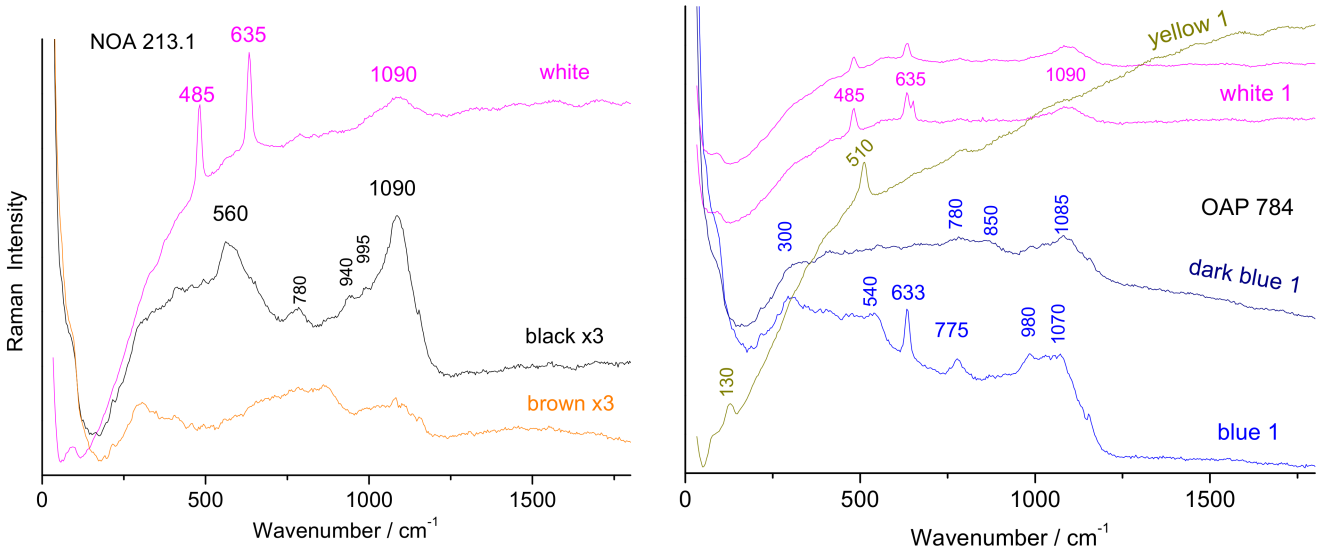


Figure 6. Representative Raman spectra recorded on different colored glass of the Spring allegory ((**a**), inv. NOA 213.1) and the Virgin with Child figures ((**b**), inv. OAP 784). The black color of NOA 213.1 is actually dark blue.

3.3. Opacifiers

The three types of opacifiers are identified and clearly observed in Raman spectroscopy: (i) calcium antimonate $Ca_2Sb_2O_7$ characterized by the Raman doublet at 485 and 635 cm^{-1} [31]; (ii) cassiterite SnO_2, characterized by the Raman doublet at 635 and 775 cm^{-1} (Figure 6) [8]; and (iii) lead, sodium, and potassium arsenate apatite ($Na_{1-x}K_xPb_4(AsO_4)_3$), characterized by the doublet at 780 and 815 cm^{-1}. Broader bands attributed to As-O stretching modes are observed between 810 and 830 cm^{-1} for other types of lead arsenates of unknown structure [12,32,33] (Figure 7). Rutile (TiO_2) opacification (doublet at 445 and 610 cm^{-1} [34], Figure 7) is also observed in restored parts.

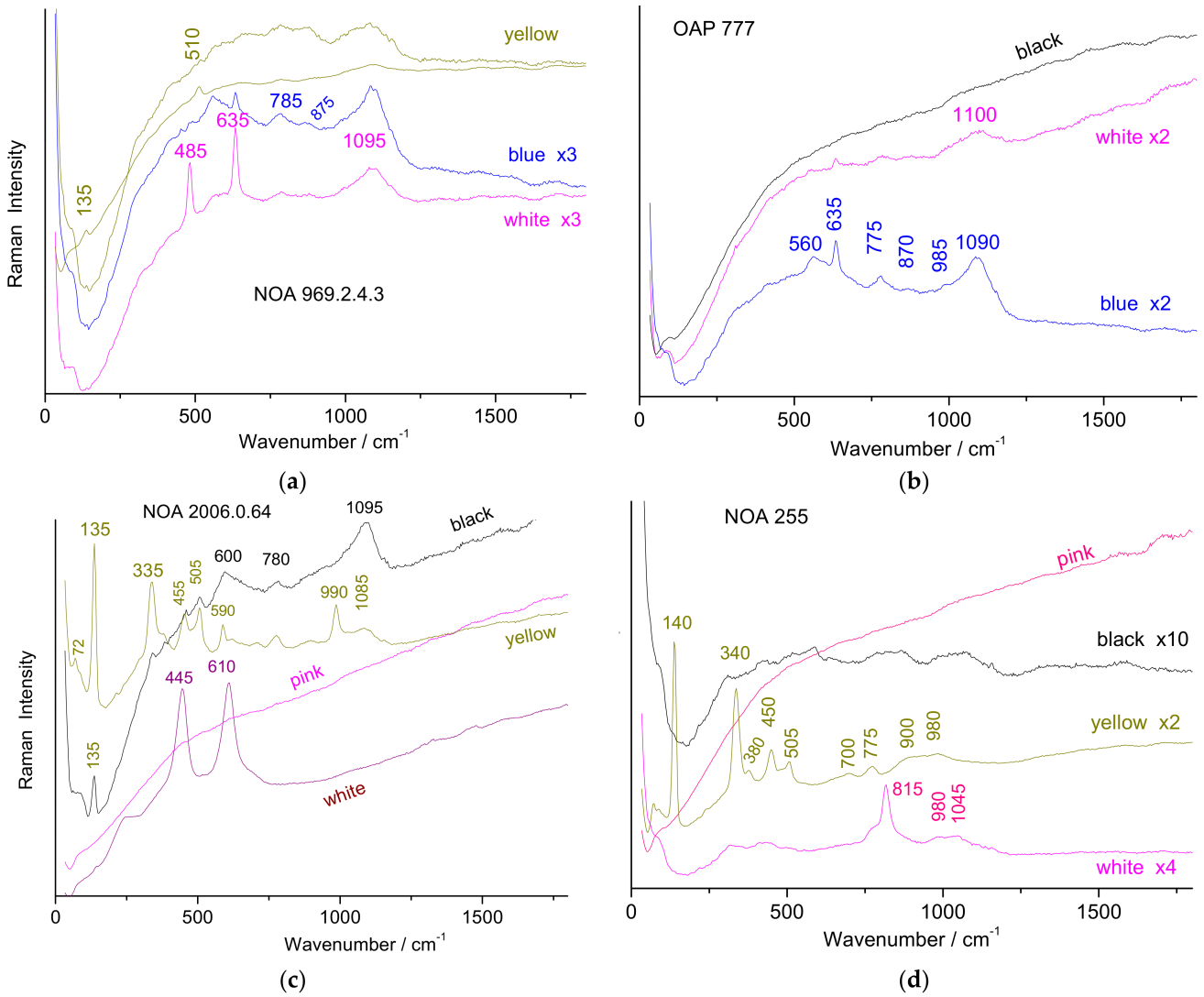


Figure 7. Representative Raman spectra recorded on different colored glass of the St. Jerome ((**a**), inv. 2006.0.643, 3rd quarter of the 17th c.), Pomone ((**b**), inv. OAP 777, 3rd quarter of the 17th c.), Shepherd ((**c**), inv. NA 969.2.4, 4th quarter of the 18th c.), and the Gosling merchant ((**d**), inv. NOA 255, 4th quarter of the 18th c.).

The identification of arsenic-based opacification is, as usual, more challenging using XRF, since the main Kα peak of arsenic (10.54 keV) [35] overlaps, given the instrumental resolution, with the Lα transition of lead (10.55 keV). Because arsenates have a strong opacifying power, the corresponding Kβ peak (11.73 keV) is consistently weak. In addition, some tin- and antimony-like ions may be dissolved within the glass network (i.e., they do not form cassiterite precipitates), which can lead to the misinterpretation of their role. For instance, in the XRF spectrum (Figure 8) of the 'Gosling merchant' (inv. NOA 255), weak peaks of arsenic, tin, and antimony are observed; however, Raman analysis demonstrates that only arsenic precipitates are responsible for the opacification of the glassy matrix.

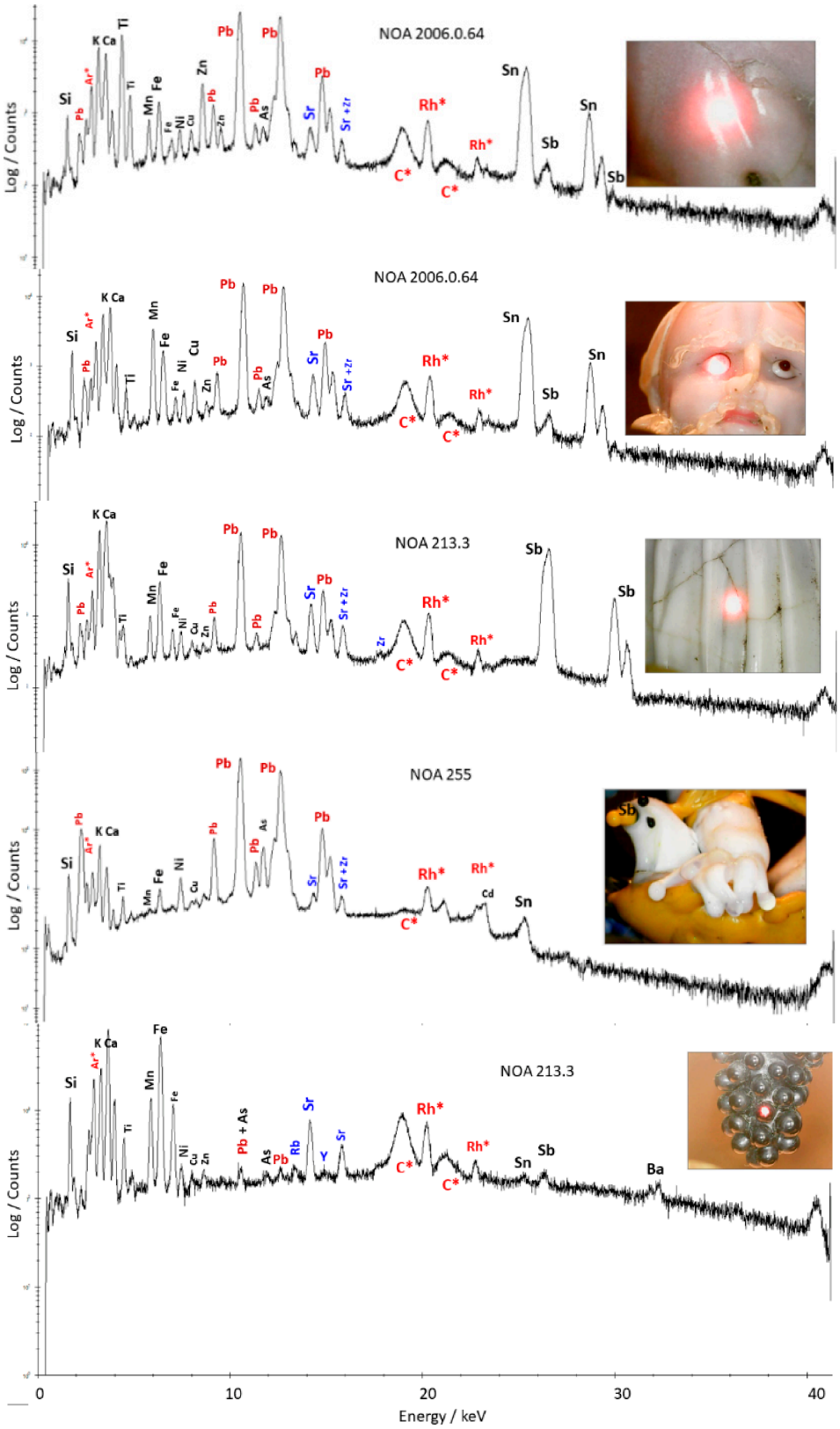


Figure 8. Comparison of the XRF spectra obtained on white and black glass for the figurines of St. Jerome (top, inv. NOA 2006.0.64, 3rd quarter of the 17th c.), the Gosling merchant (center, inv. NOA 355, 4th quarter of the 18th c.), and the allegory of Autumn (bottom, inv. NOA 213.3, 4th quarter of the 17th c.).

Examination of the ternary diagrams in Figure 9 (As-Sn-Sb, Pb-Sn-Si, and Pb-Sn-Ba) confirms the use of three types of opacifiers, based respectively on arsenic, tin, and antimony.

Barium appears as an impurity in certain objects. Notably, even black glass may contain a white opacifier.

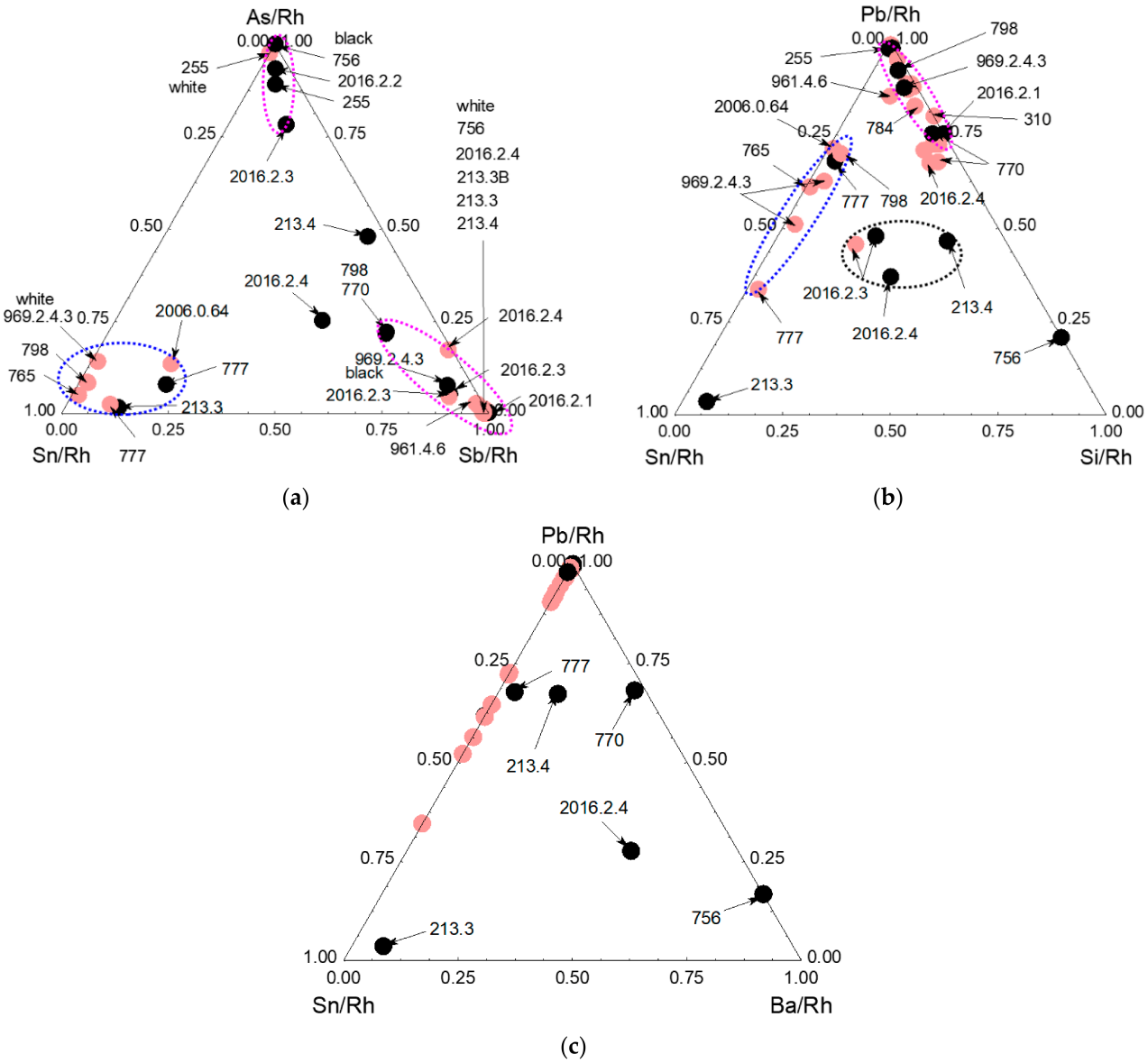


Figure 9. Sn-Sb-As (**a**), Pb-Sn-Si (**b**) and Pb-Sn-Ba (**c**) ternary diagrams constructed from the corresponding element peak areas of white (pale pink dots) and black (black dots) areas.

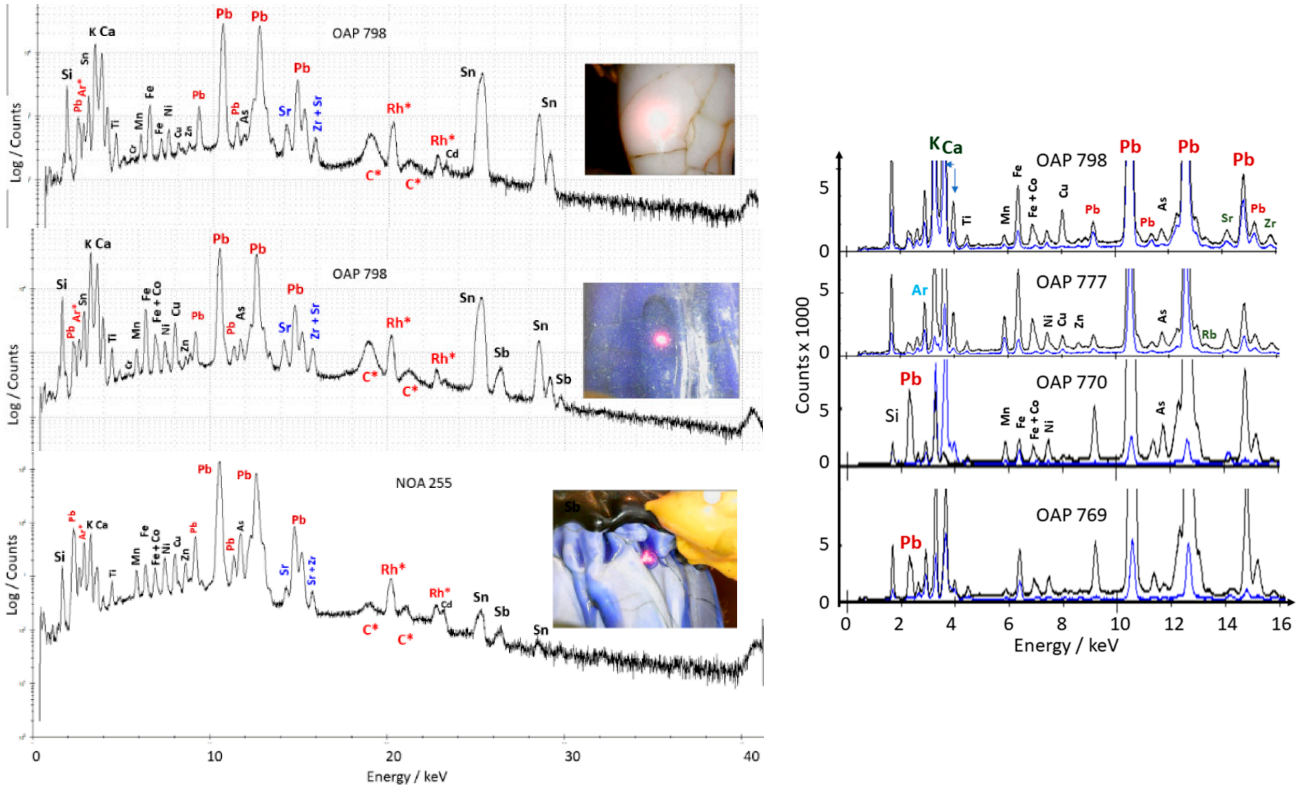
3.4. Cobalt Sources

The deposits enabling cobalt exploitation in Europe are typically mines where cobalt occurs as a by-product of the extraction of ores rich in silver, copper, arsenic, or bismuth [36,37]. Consequently, the principal source of cobalt is generally a potassium glass, known as smalt, which may contain up to 20 wt% CoO. Smalt is produced by melting the slag (residue also called *saffre*, sometimes mixed with silica) formed during the high-temperature extraction of silver, copper, or bismuth ores, or through the thermal sublimation of arsenic ores [37–41].

The semi-quantitative evaluation (based on comparison of the characteristic peak areas of each element) of elements associated with cobalt therefore provides a signature of both the geological mining context and the selection and purification processes. According to current knowledge, purification processes were developed during the 18th century and be-

came truly effective after 1850 with the rise of the industrial production of chemicals [37,38]. The content of associated elements can be comparable to that of cobalt.

Figure 10 presents representative spectra illustrating the diversity of elements associated with cobalt, including Mn, Fe, Ni, Cu, Zn, Cr, and As.



(**a**) (**b**)

Figure 10. Comparison of XRF spectra recorded on blue and white glass ((**a**), logarithmic scale; right: linear scale) for some figurines (OAP 798, NOA 255, OAP 777, OAP 770, and OAP 769; see Table 1 for details). On the right (**b**), comparison between spectra recorded on blue (stronger black spectrum) and white (weaker blue spectrum); the intensity of the white spectra is divided by two for better comparison.

We first observe the significant variation in the lead content of white opacified glasses, as already noted, in contrast to the more limited variation observed for blue glasses. Visually, the Mn/Fe, Fe/Cu, Co/Ni, and Co/As ratios are highly variable, indicating that quantitative comparison based on peak-area fitting is essential. The 'simple' approach of merely assessing the presence or absence of elements associated with cobalt, as initially proposed by Gratuze et al. [42,43], is therefore insufficient.

Due to the use of a green excitation laser in Raman spectroscopy, spectra obtained from blue glass (i.e., glass that absorbs red light) are of good quality. This is because the glass absorbs most of the fluorescence background, which occurs in the red region (>500 cm^{-1} on the Raman scale), as illustrated in Figures 6 and 7.

Examination of the ternary diagrams in Figure 11 (Co-Mn-As, Cu-Ni-As, Zn-Sn-Sb, and Fe-Sn-Sb) confirms the use of different cobalt ores. Most sources are arsenic-rich; however, in one case (OAP 784), the cobalt is associated with copper (copper-rich cobalts are characteristic of the first part of the 17th century [37]); in two cases (NOA 213.1 and NOA 310), with nickel; and in one case (NOA 255), with zinc. The presence of tin is also clearly identified for many artifacts. Some blue colored areas are poor in iron; since iron is a common impurity, it is not possible to attribute the detected iron specifically to cobalt.

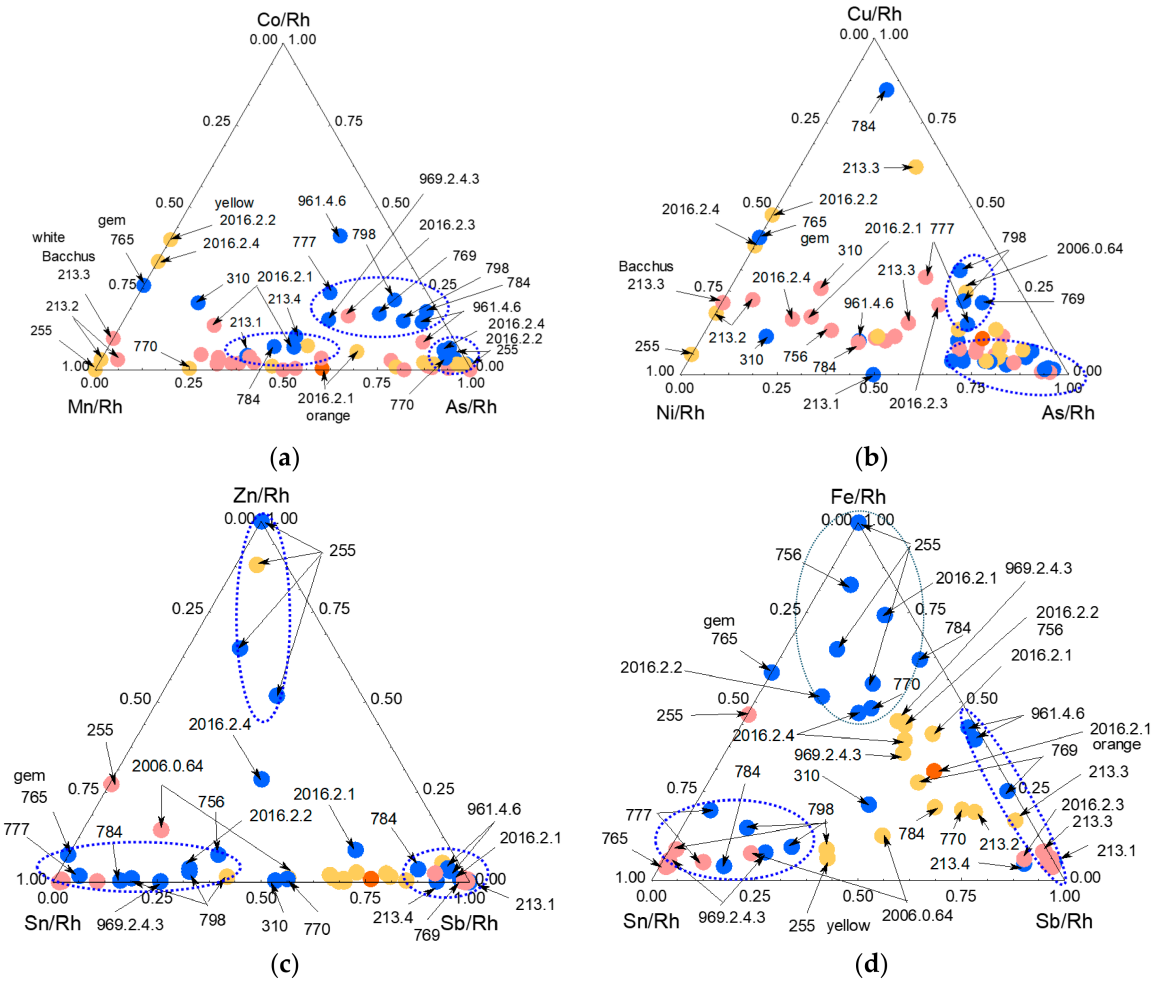


Figure 11. Co-Mn-As (**a**), Cu-Ni-As (**b**), Zn-Sn-Sb (**c**) and Fe-Sn-Sb (**d**) ternary diagrams constructed from the corresponding element peak areas of blue (blue dots), white (pink dots), and yellow areas (yellow dots) (all normalized to the Rh signal).

3.5. Yellow Pigments

Figure 12 compares the XRF spectra of a lemon yellow (inv. OAP 798) and an orange yellow (inv. NOA 255); the Sn/Sb ratios are different, as are the intensities of the zinc signals. In fact, the family of lead yellows (Naples yellows) includes two types of structures, each of which can be divided into two subgroups, respectively rich in tin (types $Pb_2Sn_2O_6$ and Pb_2SnO_4) or in antimony (types $Pb_2Sb_{2-x}Sn_xO_7$ and $Pb_2Sb_{2-x-y}Sn_yZn_xO_{7-\delta}$), but which can also both be partially substituted by Fe and Si [44–49].

The zinc signal is easily measured, but it is not possible to separate by XRF the iron or silicon included in the pigment from those already present in the silicate matrix. The types of pigment are, however, very easily distinguished by Raman scattering depending on the position of the intense translational mode of the Pb^{2+} ions between 125 and 140 cm^{-1}, and the presence or absence of Raman peaks at 200, 330, 450 and 510 cm^{-1} [48,49]. The 510 cm^{-1} peak, usually assigned to the Sb-O stretching mode, is characteristic of lead–antimony Naples yellow. However, the significant non-stoichiometry and extensive partial substitution within the pyrochlore solid solution make detailed assignment complex and beyond the scope of this study (see references [44–49]).

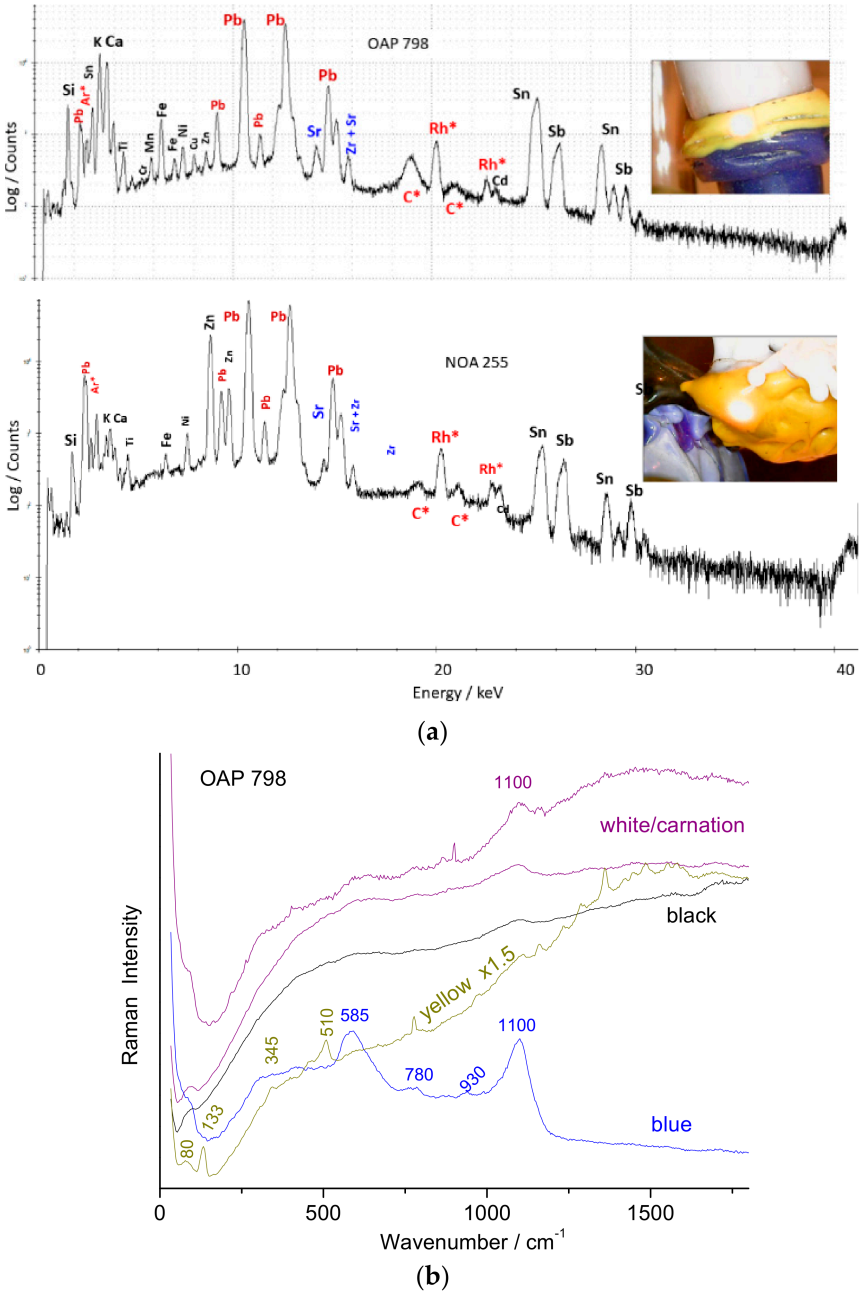


Figure 12. Comparison of XRF spectra recorded from the yellow areas of OAP 798 and NOA 255 figurines. The Raman spectrum of OAP 798 artifact is given. See Figure 7 for the Raman spectrum of the NOA 255 ware.

Thus, for the yellows of the figurines OAP 798 (XRF and Raman: Figure 12) and NOA 255 (XRF: Figure 12; Raman: Figure 7), the two main types of yellow pigment based on lead, tin, and antimony are observed. Differentiation is obvious by comparing the respective intensity of the 510 cm^{-1} peaks (Sb-O stretching mode characteristic of antimony-rich pyrochlore) versus the ca. 135–140 cm^{-1} peak (Pb^{2+} ion T′ mode) [49].

Examination of the ternary diagrams in Figure 11 (Zn-Sn-Sb and Fe-Sn-Sb) confirms the use of a mixed antimony–tin pigment, with some partial substitution by iron. Tin-rich compositions are rare (OAP 798, NOA 255, and NOA 2006.0.64). The amount of pigment varies depending on the analyzed spot. NOA 255 is the only sample that uses a Zn-rich Naples yellow pigment.

3.6. Pink, Black and Brown

Figure 13 shows the Raman spectra of figurine NOA 961.4.6 ('The Good Shepherd') over the entire spectral range. We note the particular bell-shaped form of the optical spectrum (maximum at ~1700 cm^{-1}, i.e., 584.9 nm on an absolute scale) obtained on red glass, a characteristic luminescence feature due to the presence of metallic nanoparticles in the glass, implying the formation of a plasmon (electron gas) at the metal/dielectric interface, i.e., particle/silicate matrix [50]. The position (in nm) of the fluorescence band may correspond to either gold or copper nanoparticles. The plasmon energy position depends on both the nature of the metal and the size and shape of the nanoparticles; therefore, it is not possible to unambiguously identify the metal responsible for the phenomenon [50,51].

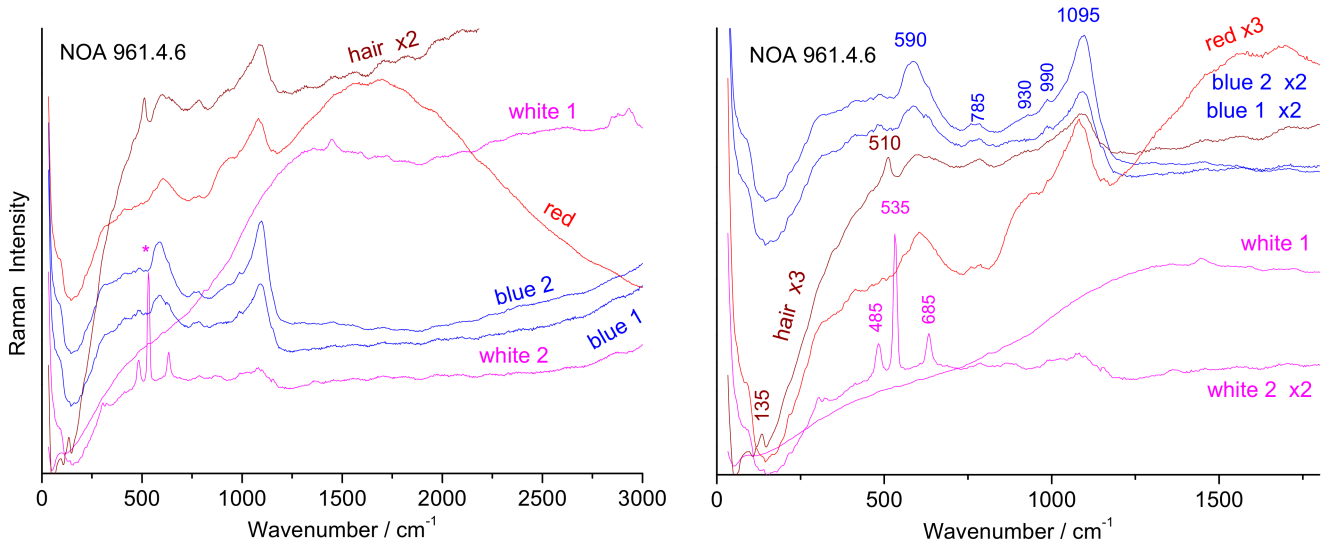


Figure 13. Raman spectra over the full recorded spectral range and a zoom on the region related to the vibrational signature of NOA 961.4.6; see Figure 4 for the corresponding XRF spectrum of the red glass.

Due to the very high coloring power of metal nanoparticles (typically 0.1 wt% M° is sufficient for strong coloring) and the small thickness of some colored layers, detection by XRF is difficult; in many cases, it is not possible to identify them via Au peaks [50]. In the NOA 961.4.6 spectrum (Figure 4), a very weak peak is observed at the limit of detection around 9.7 keV, just between a weak lead peak and the main Lα1 peak. The peaks of the Kα and Kβ transitions of copper are, on the other hand, strong, which suggests that the red color is obtained by Cu° nanoparticles, possibly together with cuprite Cu_2O, another red pigment requiring fewer reducing conditions than Cu° [51–53].

On the contrary, in the pink area of the cheek of the figurine representing King Louis XVIII (Figure 14), the copper signal is extremely weak. Gold is not directly detected, whereas the arsenic signal is relatively intense. Arsenic is known to be used in the precipitation of gold colloids for producing ruby glass [8,54], and no arsenic peak is observed in white glass (antimony-based opacification). The detection of arsenic can therefore be considered an indirect signature of the presence of gold responsible for the pink coloration.

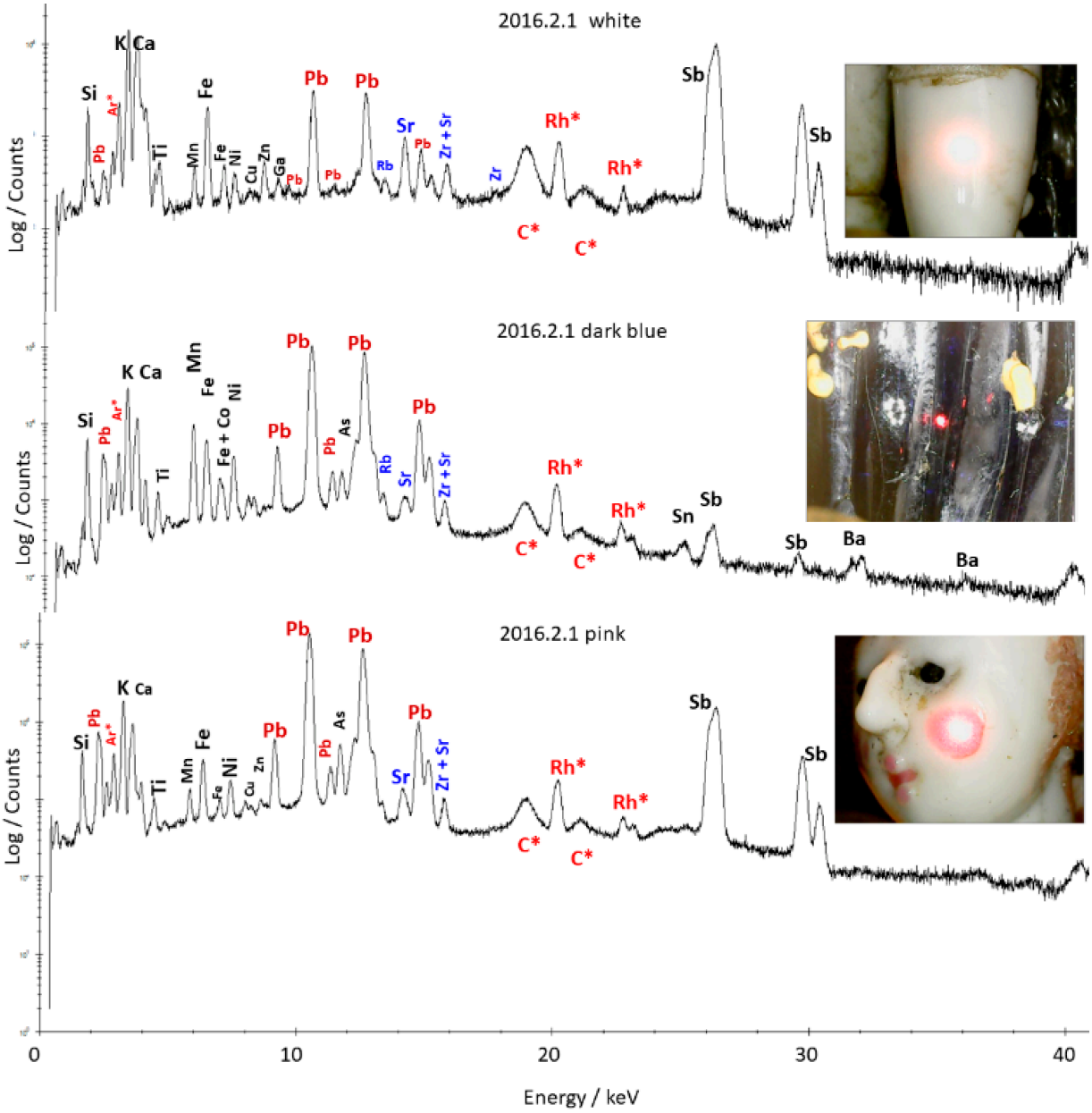


Figure 14. XRF spectra of NOA 2016.2.1. Louis XVIII figurine.

3.7. Aventurine

Aventurine glass is a reddish glass containing golden inclusions formed by copper metal crystals approximately 150–200 μm in size, dispersed within the glass matrix [40]. This characteristic appearance is observed in two objects: the dress edging of OAP 769 and NOA 213.4 (Figure 15). Copper-related transitions are intense in both cases. However, contributions from neighboring colors to the XRF spectrum complicate the interpretation of associated elements.

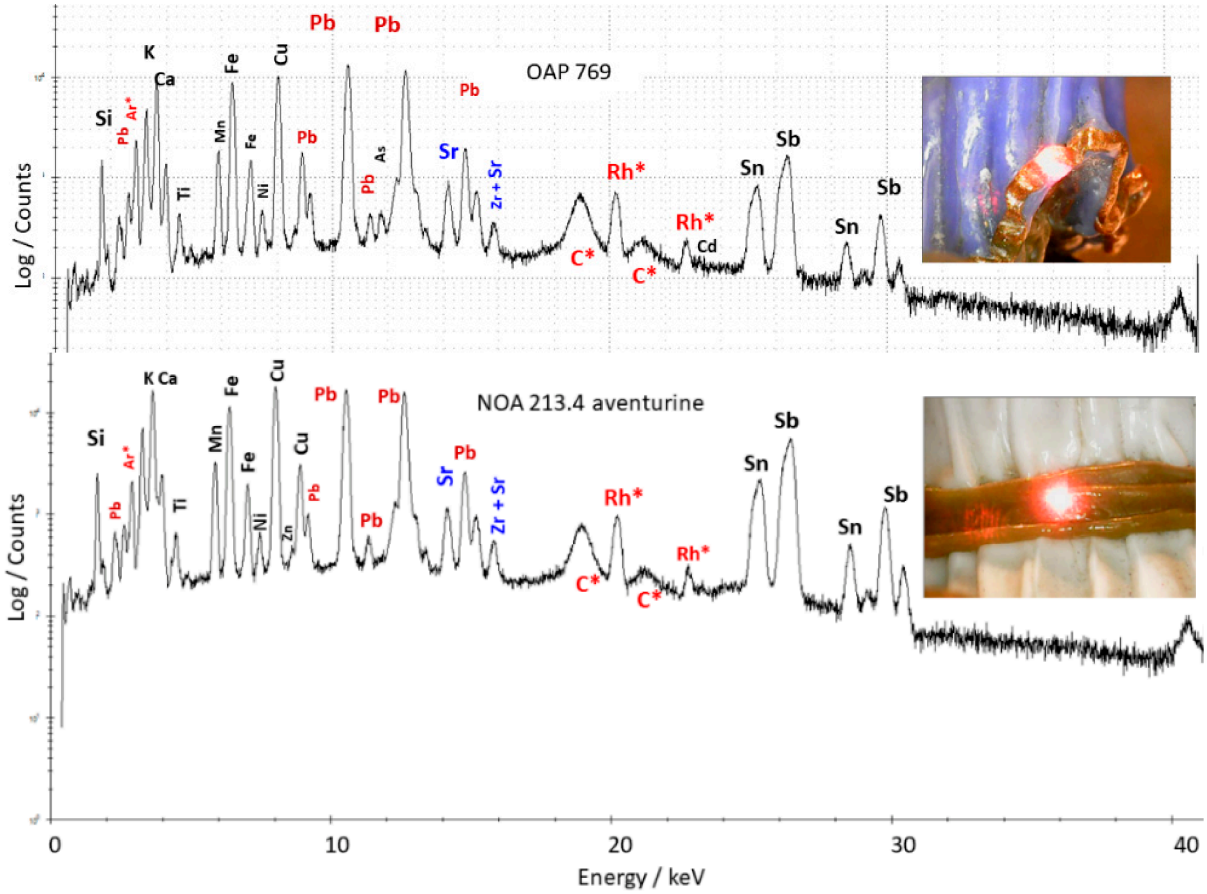


Figure 15. XRF spectra of OAP 769 et NOA 213.4 aventurine glass.

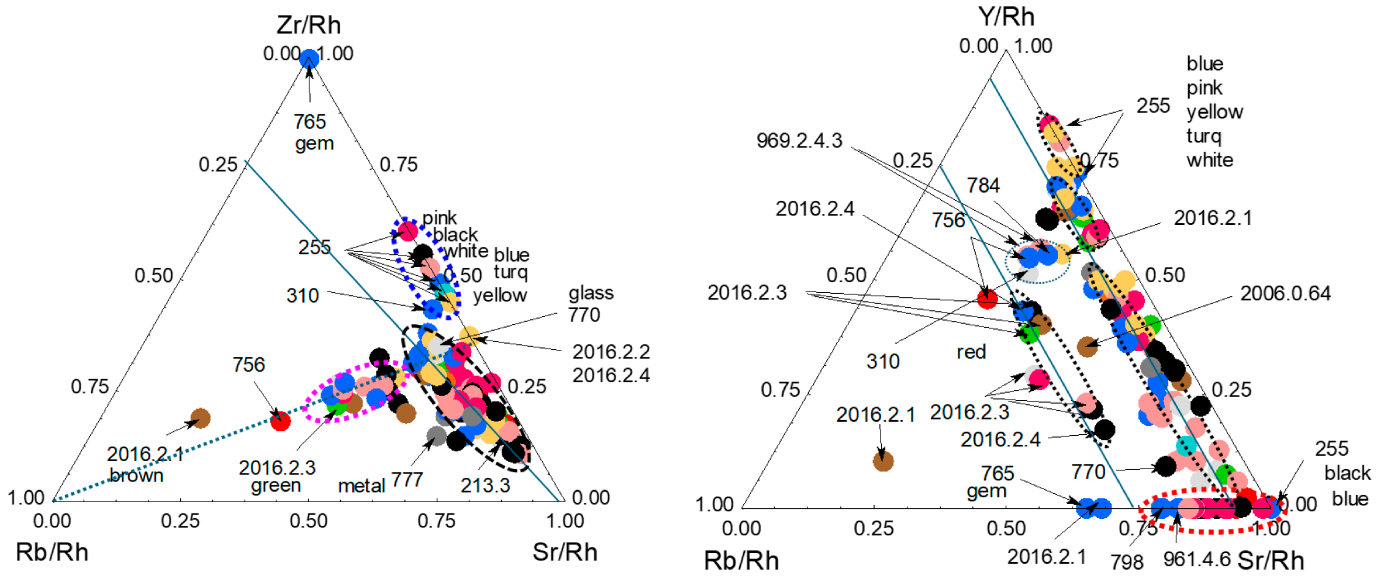
This type of glass is not mentioned in the well-known treatise *L'Arte vetraria* by Antonio Neri (1576–1614), published in 1612, but appears in a 1626 inventory referring to *pasta venturina*, and in another from 1630 as *piera venturina* [55–57]. In 1644, Giovanni Darduin's Ricettario noted that '*the production of aventurine depends more on chance than on controlled technique*'. Letters from Philipp Hainhofer (1578–1647) to Duke August zu Braunschweig-Lüneburg describe "*a kind of stone with gold stars inside*," and the arcanist Luca Tron (1552?–1620/25) is reputed to have produced this type of glass [57].

In fact, the recipe can be traced back at least to the Seljuk period (13th century), as evidenced by an amulet uncovered during the Ravy excavations in present-day Iran [55].

3.8. Rb, Sr, Y and Zr as Trace Elements

Trace elements such as rubidium (an impurity associated with sodium and potassium), strontium (a calcium impurity), yttrium (associated with zirconium), and zirconium (a quartz impurity, typically present as zircon) produce strong signals at concentrations of a few hundred ppm. They are therefore widely used to identify raw materials, fluxes (Rb, Sr), and sands (Y, Zr) [58–63]. The corresponding ternary diagrams are shown in Figure 16.

The elements Zr, Rb, and Sr are respective impurities of Si, K, and Ca, and some of this information is reflected in the diagrams in Figure 5, particularly the constant Si/flux ratio. However, characteristic groups can be observed, which are linked to the use of different raw materials. The pale blue quartz of OAP 765 is an exception: it is not glass but a gem. The data point is located at the Zr apex due to the high levels of Zr traces in many quartz samples, often in the form of zircon inclusions. The NOA 255 figurine is clearly separated from the others, indicating a different origin.

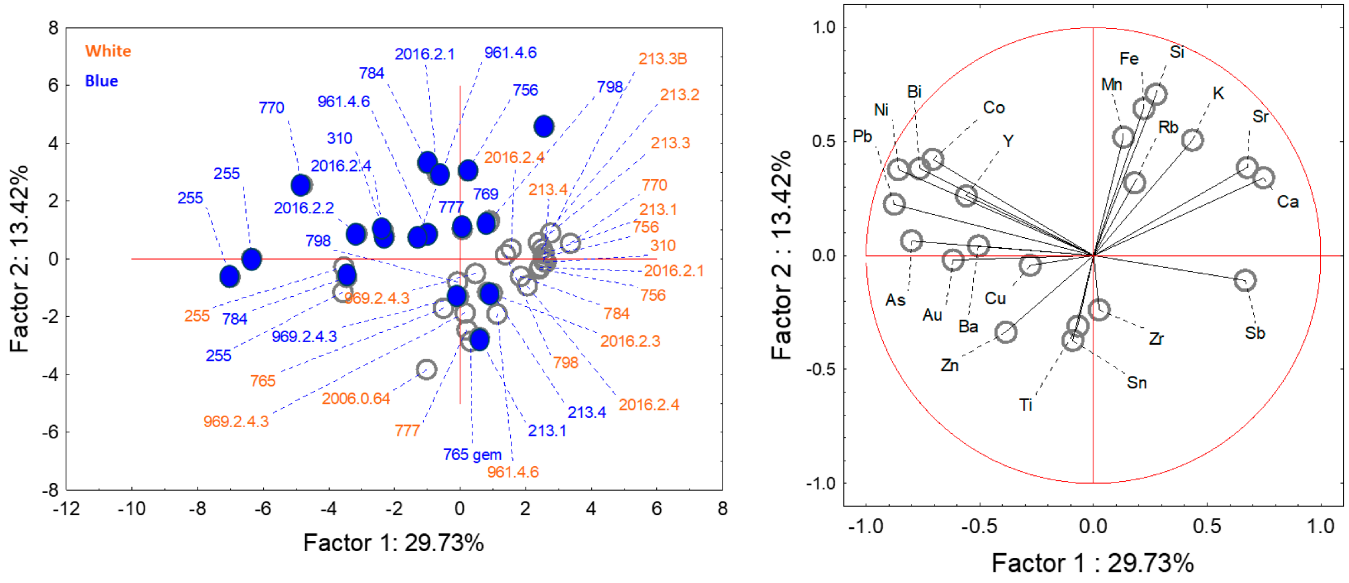


(**a**) (**b**)

Figure 16. Rb-Sr-Zr (**a**) and Rb-Sr-Y ((**b**), normalized to the Rh signal) ternary diagrams constructed from the corresponding element peak areas.

3.9. Chemometrics

Chemometrics, i.e., Principal Component Analysis (PCA) (Figures 17 and 18) and hyperspace visualization of similarity distances (Figures 19 and 20) have a long history in archaeometry since the 1980s [64–69]. This method has primarily been applied to body paste analysis due to the use of local raw materials (e.g., [64–69]) and has rarely been used for glaze elemental compositions [70]. The technique can also be applied using parameters extracted from Raman spectra [49].



(**a**) (**b**)

Figure 17. *Cont.*

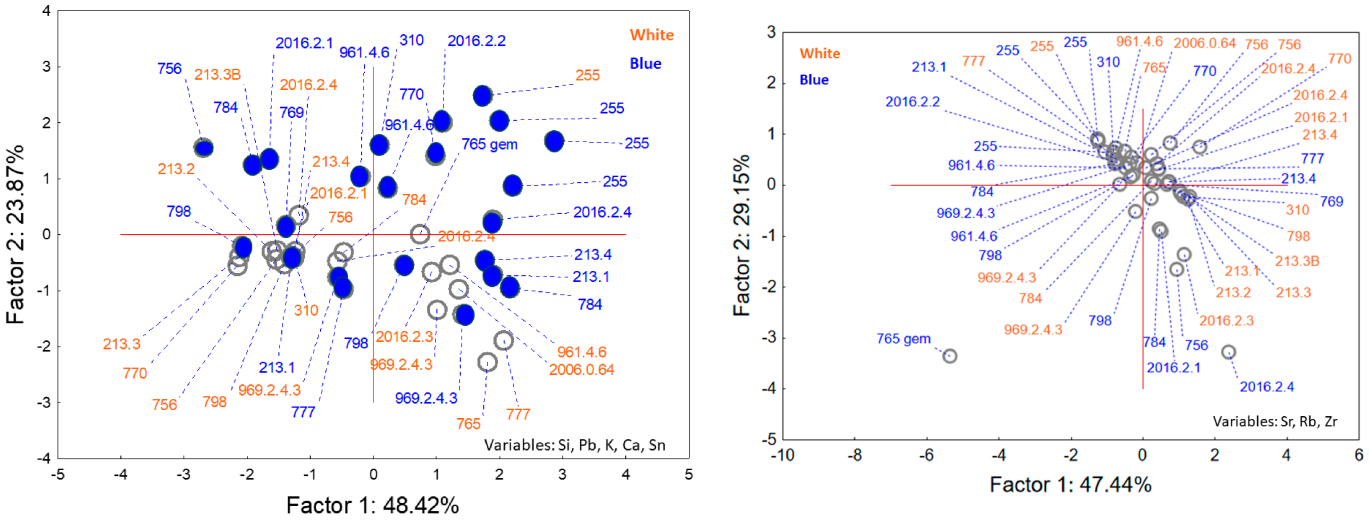


Figure 17. Comparison of PCA factor plots calculated using all elements measured with pXRF ((**a**): scores of the first factors; (**b**): corresponding loadings) and those calculated using two subsets of variables: major elements (Si, Pb, K, Ca, and Sn; (**c**)) and characteristic trace elements (Sr, Rb, and Zr; (**d**)). Artifact inventory numbers that do not belong to the main group are underlined.

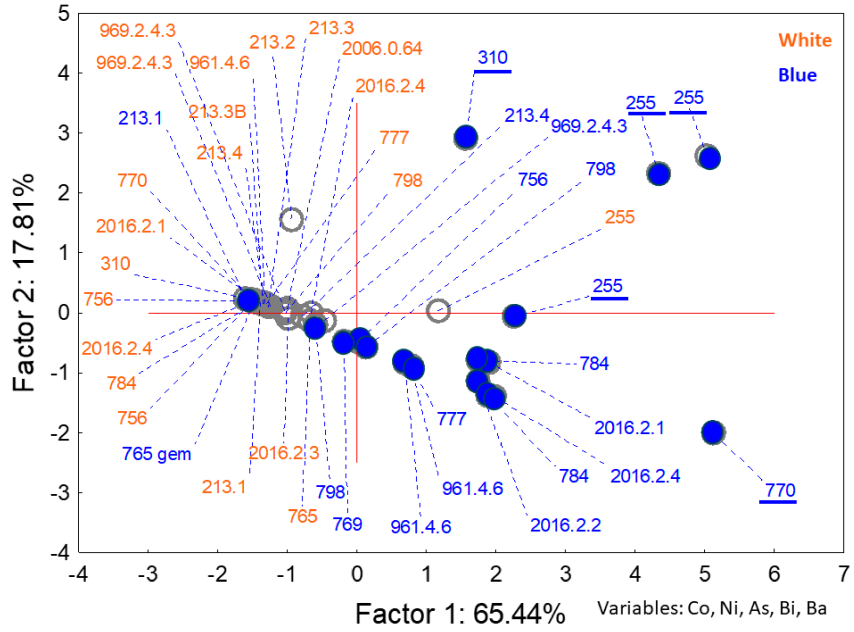


Figure 18. Comparison of PCA factor plots calculated using cobalt and associated elements as variables. Artifact inventory numbers that do not belong to the main group are underlined.

The factor plot in Figure 17a was calculated using the areas of all XRF peaks. A clear separation is observed between measurements taken on the white and blue enamel areas, along with several subgroups separated by distances greater than those observed for repeated measurements on different spots of the same color within a single object (e.g., object 255). Examination of the corresponding loading plot (Figure 17b) shows that the elements responsible for this differentiation are cobalt and its associated elements. When only these elements are used as variables, the variance explained by the first two factors increases to 48.5% and 28.9%, compared to 30% and 13% when all variables are included. Subgroups similar to those observed in Figure 11 are then identified. The plot calculated

using silica and flux-related impurities forms a well-defined cluster, with only a few outliers: the bluish quartz of 765 and the white areas of 756, 770, 784, 2016.2.4, and 2026.2.1.

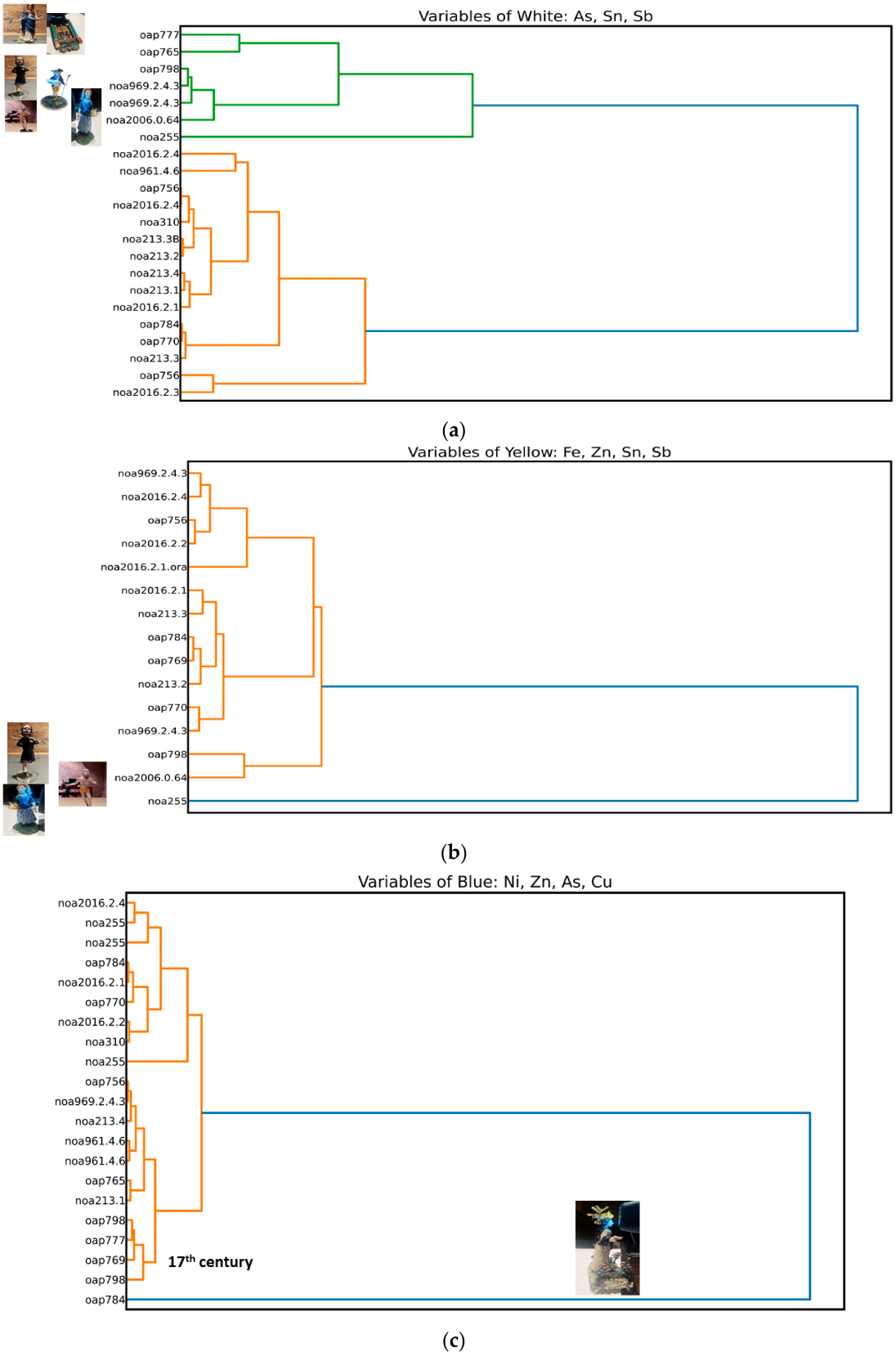


Figure 19. Ward Euclidean dendrograms of similarity built using (**a**) As, Sn, and Sb elements characteristic of white opacifiers; (**b**) Fe, Zn, Sn, and Sb, characteristic of yellow pigments; and (**c**) As, Cu, Ni, and Zn, associated with cobalt.

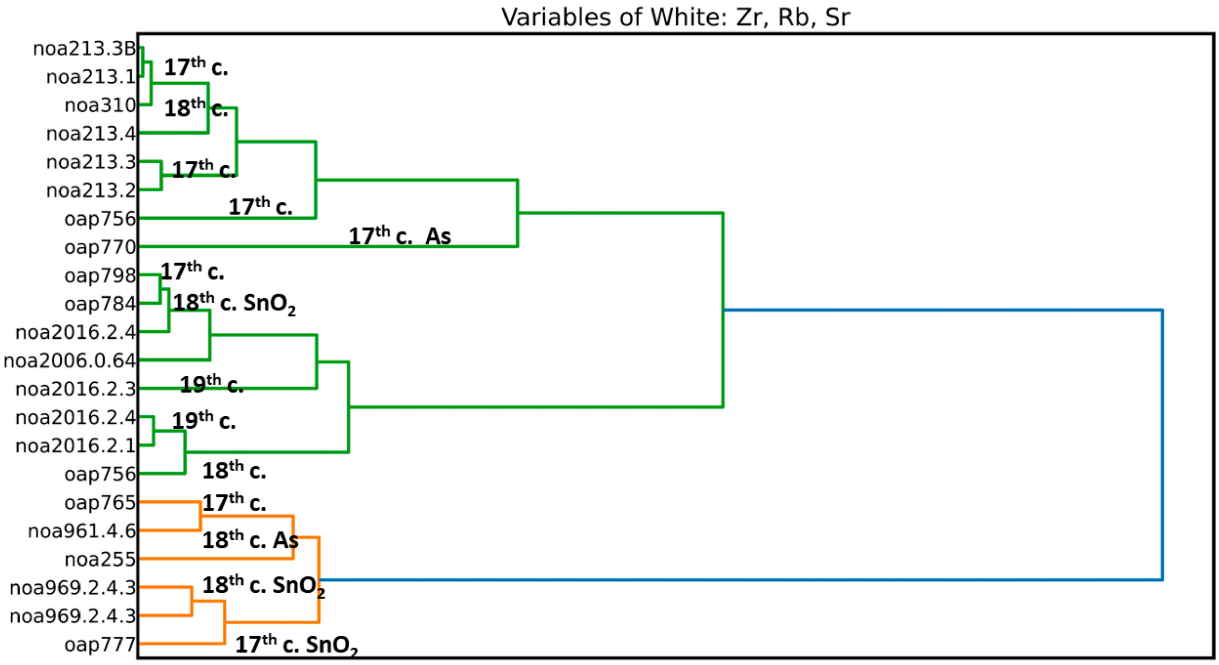


Figure 20. Ward Euclidean dendrograms of similarity constructed using the Zr, Rb, and Sr elements for white glass. Assigned dates and special characteristics of the figurines are indicated.

Figure 18 presents the factor plot calculated using signals from cobalt and its main associated elements. In addition to the expected separation between measurements taken on blue and white areas, several outlying objects are identified, namely 310, 255, and 770. Artifacts 784, 2016.2.1, 2016.2.4, and 2016.2.2 form a distinct subgroup separate from the main cluster.

The construction of PCA factor plots does not provide additional information beyond that obtained through the reasoned approach. The origins of the data clustering can be directly interpreted from ternary diagrams, owing to the well-established relevance of impurity levels, such as Zr and Y for silicates, Rb and Sr for fluxes, and Mn, As, Fe, and Ni, as well as Bi, Cu, and Ag, for cobalt.

Similarity-distance algorithms generally yield results comparable to visual examination of spectra, but they require testing multiple variables. In contrast, examination of ternary diagrams hierarchizes the relative importance of different parameters and provides an overview of data dispersion.

The dendrogram obtained using peak areas of elements associated with different opacification methods (Figure 19a,b) clearly distinguishes the figurines OAP 777, OAP 765, OAP 798, NOA 969.2.4.3, and NOA 2006.0.64. The dendrogram for yellow pigments identifies NOA 255, NOA 2006.0.64, and OAP 798. The dendrogram of elements associated with cobalt, As, Ni, Zn, and Cu (Figure 19c) highlights OAP 784 and early Nevers production objects (OAP 798, OAP 777, and OAP 769), reinforcing these attributions.

Similarity dendrograms based on peak areas of impurities characteristic of sand (Zr, Y) and fluxes (Ca: Sr; alkalis: Rb) are shown in Figure 20 for white glass. Most figurines already identified as different form a distinct group (OAP 765, NOA 255, OAP 777, NOA 969.2.4.3). This confirms the presence of figurines from two different origins. However, since the glass rods used to make these sculptures were likely imported, possibly from Venice rather than produced in Nevers, the identification of separate groups primarily reflects different manufacturing procedures and workshops, which may have been located in Nevers or other cities. Notably, there is no correlation between these groupings and the stylistically attributed production dates.

4. Discussion

4.1. Compositional Variability

Few compositional data are available in previous publications, but these also demonstrate a large dispersion of compositions, even within the same color (Table 2). Opacifiers are highly variable, as are their quantities. The use of cassiterite is observed for objects attributed to Orléans, often accompanied by higher lead contents. The results obtained, clearly visible in Figure 5, confirm the limited data in the literature, although this variability has not previously been highlighted or discussed.

Table 2. Variety of glass compositions measured for Nevers [10] and Orléans [44] glass (-: not measured/compared).

	Nevers [9–11]				Orléans [8,63]							
	NG69	**NG75**	**NG1**	**Eros**								
Color	**Green**	**Green**	**Green**	**White**	**White**	**White**	**White**	**White**	**Red**	**Green**	**Yellow**	**Blue**
SiO_2	55.2	62.6	61.7	81.2	44.7	58	77	64	38	34	36	47
Al_2O_3	0.3	0.6	0.1	0.2	0.27	-	-	-	-	-	-	-
MgO	1.1	2.7	1.2	0.36	0.34	-	-	-	-	-	-	-
Na_2O	4.8	8.5	13.9	0.14	2.07	-	-	-	-	-	-	-
K_2O	11.1	8.1	8.9	6.79	11.77	17	8	14	4	2	3	9
CaO	4.9	7.2	4.7	1.37	1.33	14	4	12	2	1	2	2
PbO	15.4	5.3	5.5	9.1	37.9	-	4	-	38	55	44	30
Fe_2O_3	0.2	0.6	0.2	0.1	0.14	-	-	-	-	-	-	-
Sb_2O_3	0.3	0.7	0.7	0.01	0.07	5	3		2	1	1	
MnO	-	0.1	-	0.07	0.05	-	-	-	-	-	-	-
CuO	6	2	3.4	0.005	0.03	-	-	-	-	-	-	-
SnO_2	-	-	-	-	-	-	-	-	13	7	12	9
P_2O_5	-	-	-	-	-	6	3	10	-	-	-	-
As_2O_3	-	-	-	-	-	-	1	-	-	-	-	1
SO_3	0.4	0.7	-	-	-	-	-	-	-	-	-	-
Cl	0.6	0.7	-	0.17	0.98	-	-	-	-	-	-	-
	100.3	99.8	100.3	99.5	99.65	100	100	100	97	100	98	98

This compositional variability is unusual, as the composition of fire-art objects is characteristic of a specific production (place and period). It appears to be linked to the special manufacturing technique of these glass 'sculptures', which renders each figurine unique. The use of lamp-flame working requires low-melting-point glasses. Published compositions often do not account for elements such as boron and lithium introduced via borax (which also contributes a small amount of sodium [71]). These elements are difficult to detect with both invasive/destructive analytical techniques (LA-ICP-MS, LIBS) and non-invasives ones (PIGE/PIXE) [72–81], and some likely evaporate during hot working. If these elements are present, the compositional variability is likely even greater than observed.

4.2. Technical Constraints and Comparison with Perrot's Workshop Production

Several questions arise. The process begins with glass rods, whose composition likely varies depending on their origin and color. Yellow glasses colored with lead–tin, lead–antimony pigments, or their combinations are very lead-rich; the same applies to pink and red glasses colored by metallic nanoparticles as observed in glass and enameled artifacts [70]. White opacified glasses may, however, be lead-free (Table 3).

Depending on the part of the figurine and the skill of the craftsman, the viscosity of the glass paste must vary. This likely required the addition of extra flux by combining different rods, which explains the exceptional variety of compositions observed.

Four categories can be defined based on Pb content: (i) Pb-rich group: Pb peak is higher than K and Ca peaks (according to the literature, the Pb content can reach up to 60 wt%); (ii) Pb-poor group: Pb peak is lower than K and Ca (~5 wt % PbO); (iii) intermediate group: Pb and K/Ca peak hights are comparable; (iv) Pb-free (or trace Pb) group. Comparison is difficult when the colored area is small and neighboring material contributes to the spectrum (and calculation of a composition is not possible).

Table 3. Summary of glass characteristics (artifacts different from the others are in bold or underlined; empty boxes indicate that no measurement was performed).

	Artifact	Opacifier		Pigment/Colorant Agent and Associated Elements		Date	Remarks
		Raman	XRF	Raman	XRF		
Colorless	OAP 770		K,Ca			17th	No Pb
	NOA 2006.0.64		Sn			17th	Pb glass
	NOA 213.2		no			17th	Pb-rich glass
	NOA 213.3		K,Ca			17th	No Pb
	NOA 213.4					17th	Pb-rich glass
	NOA 20216.2.3					19th	Pb glass
White	OAP 798		Sn			17th	Pb
	OAP 769		Sb,As			17th	Pb glass
	OAP 770	$Ca_2Sb_2O_7$	Sb			17th	Pb glass
	OAP 777	SnO_2	Sn			17th	Pb-rich glass
	NOA 2006.0.64	TiO_2	Ti,Sn,As			17th	Restored? Pb glass
	NOA 213.1	$Ca_2Sb_2O_7$	Sb			17th	Pb-rich glass
	NOA 213.2		Sb			17th	Pb-rich glass
	NOA 213.2		Sb,Sn			17th	Pb-rich glass
	NOA 213.3	$Ca_2Sb_2O_7$	Sb			17th	Pb glass
	NOA 213.4	$Ca_2Sb_2O_7$	Sb			17th	Pb glass
	NOA 961.4.6	$Ca_2Sb_2O_7$					
	NOA 969.2.4.3	$Ca_2Sb_2O_7$	Sn			18th	Pb glass
	OAP 784	$Ca_2Sb_2O_7$	Sb			18th	Pb glass
	NOA 310	$Ca_2Sb_2O_7$	Sb,Sn		Co	18th	Pb-rich glass
	NOA 255	**As-apatite**			As	18th	Pb-rich glass
	NOA 756	$Ca_2Sb_2O_7$	Sb		Sb		Pb poor glass
	NOA 2016.2.1	$Ca_2Sb_2O_7$	Sb			19th	Pb-poor glass
	NOA 2026.2.2		Sb			19th	Pb-rich glass
	NOA 2026.2.3		Sb			19th	Pb-poor glass
	NOA 2016.2.4		Sb			19th	Pb glass
	OAP 765		Sn				Pb-rich glass

Table 3. *Cont.*

	Artifact	Opacifier		Pigment/Colorant Agent and Associated Elements		Date	Remarks
Blue	OAP 798		Sn,Sb		Co,As	17th	Pb glass
	OAP 769	$Ca_2Sb_2O_7$	Sb		Co,As	17th	Pb glass
	OAP 770	**As-based**	**Sn**		Co,As	17th	Pb-rich glass
	OAP 777	SnO_2	Sn		Co,As	17th	Pb glass
	NOA 213.4		?		Co,As	17th	?
	NOA 961.4.6	($Ca_2Sb_2O_7$)	Sb		Co,As	17th	Pb-rich glass
	NOA 969.2.4.3	SnO_2	Sn,Sb		Co,As	18th	Pb glass
	OAP 784	no	Sb		Co,As,Mn,Ni	18th	Pb glass
	OAP 784	SnO_2	Sn,Sb		Co,Cu,As	18th	Pb-rich glass
	NOA 310	$Ca_2Sb_2O_7$	Sn,Sb		Co, ?	18th	Pb poor glass
	NOA 255		As		Co,AS,Ni	18th	Pb-rich glass
	NOA 255		As		Co,As,cu	18th	Pb-rich glass
	OAP 756				Mn,Co,As	18th	Pb-rich glass
	NOA 2026.2.1				Mn,Co,As	19th	Pb-glass
	NOA 2016.2.2				Co,As	19th	Pb-rich glass
	NOA 2016.2.4				Co,As	19th	Pb-rich glass
	OAP 765				Cu		No Pb (turquoise)
Yellow	OAP 798			PbSb NY	Sn,Sb,Zn	17th	Pb-rich glass
	OAP 769			PbSb NY	Sn,Sb	17th	Pb-rich glass
	OAP 770			$Pb_2Sb_{2-x}Sn_xO_7$	Sb,Sn	17th	Pb-rich glass
	OAP 770	As-based	-		-	17th	Pb-rich glass
	OAP 770	**$Ca_3(PO_4)_2$**		$Pb_2Sb_{2-x}Sn_xO_7$	Sn,Sb	17th	Pb-rich glass
	NOA 213.3			$Pb_2Sb_{2-x}Sn_xO_7$	Sb,Cu,Zn	17th	Pb-rich glass
	NOA 969.2.4.3			$Pb_2Sb_{2-x}Sn_xO_7$	Sb,Sn,Fe	18th	Pb-rich glass
	OAP 784			$Pb_2Sb_{2-x}Sn_xO_7$	Sb,Sn,Zn	18th	Pb-rich glass
	NOA 255			$Pb_2Sb_{2-x-y}Sn_xZn_yO_7$	Sn,Sb,Zn	18th	Pb-rich glass
	NOA 756			$Pb_2Sb_{2-x}Sn_xO_7$	Sn,Sb	18th	Pb-rich glass
	NOA 2016.2.1				Fe,Sb	19th	Pb-rich glass (orange)
	NOA 2016.2.2				Sb,Sn,Fe		Pb-rich glass
	NOA 2026.2.4				Sn,Sb		Pb-rich glass
Brown	NOA 2006.0.64		Sn,Sb		Mn,Fe	17th	Pb glass
	NOA 961.4.6		Sb		Mn,Fe	17th	Pb-rich glass
	NOA 2016.2.1		Sb		Fe	19th	No Pb
	NOA 2016.2.3		Sb		Mn,Fe	19th	Pb-poor glass

Table 3. *Cont.*

	Artifact	Opacifier		Pigment/Colorant Agent and Associated Elements	Date	Remarks
Black	OAP 798			Mn	17th	Pb glass
	OAP 770			Mn,Fe, Ba	17th	Pb-poor glass
	OAP 777		Sb	Mn	17th	Pb glass
	NOA 2006.0.64		Sn	Mn	17th	Pb glass
	NOA 213.3			Fe	17th	No Pb
	NOA 213.4			Mn,Fe	17th	No Pb
	NOA 969.2.4.3		Sb	Mn,Fe	18th	Pb glass
	OAP 756			Mn,Fe	18th	No Pb
	2016.2.2			Fe,Mn,Ba	19th	No Pb
	2016.2.3		Sb	Mn		Pb-rich glass
Aventurine	OAP 769		Sb,Sn	Cu	17th	Pb-rich glass
	NOA 213.4		Sb,Sn	Cu	1èth	Pb glass17th
Pink	OAP 777		Sn	Mn,Cu	17th	Pb-rich glass
	NOA 2006.0.64		Sn	Cu,Zn,As	17th	Pb glass
	NOA 213.1		Sn,Sb	?	17th	Pb-rich glass
	NOA 213.2		Sb,Sn	As ?,Cu	17th	Pb-rich glass
	NOA 213.3		Sb,Sn	?	17th	Pb-rich glass
	NOA 310	As-based, Fluorescence	Sb	As	18th	Pb-rich glass
	NOA 255	Fluorescence		As		Pb-rich glass
	OA 756	**Fluorescence As-based**	**Sb,As**	As	18th	Pb-rich glass
	NOA 2016.2.1		Sb	As	19th	Pb-rich glass
	NOA 2016.2.3		Sb	As	19th	Pb glass
Red	NOA 961.4.6	Fluorescence		Cu,Fe	17th	No Pb
Grey	NOA 2555			Cu,Mn,As,Ni	18th	Pb-rich glass
Green	NOA 213.1		Sn	Cu	17th	Pb-rich glass
	NOA 213.2		Sb,Sn	Cu ?	17th	Pb-rich glass
	NOA 310		Sb	Cu,As		Pb-rich glass
	NOA 756		Sb	Cu		No Pb

Based on previous studies showing the significant use of cassiterite as an opacifier in Orléans [8,81], three objects using this technique (Table 3: two figurines dated to the 18th century (NOA 969.2.4.3 and OAP 784) and one to the 17th century (OAP 777)) are possibly of Orléans origin. The OAP 255 (18th c.) and OAP 770 (17th c.) figurines are characterized by arsenic and/or bone-based opacification, indicating a different workshop/origin.

4.3. Pink and Carnation

Strong fluorescence signals indicate the presence of metallic nanoparticles. Due to their high plasmonic coloring power, gold or copper quantities below 0.1 wt % are sufficient, making gold detection by pXRF difficult. On the other hand, the detection of certain elements incorporated during the preparation of gold nanoparticles by precipitation from an *aqua regia* solution [13,50,51] may be easier. This is the case for arsenic, which can be detected relatively easily by pXRF and very effectively by Raman micro-spectroscopy due to the strong As-O stretching modes. Tin is also well detected by XRF, and cassiterite by Raman scattering. For other elements, such as antimony and iron [13], it is more difficult to determine whether they are associated with gold, present as constant impurities (Fe), or used as opacifiers (Sb or Sn). Indeed, the collimation of the X-ray beam is often insufficient to avoid contributions from neighboring colors.

Although no XRF signal characteristic of gold is clearly observable, the presence of a plasmon luminescence band close to 584.9 nm (1700 cm^{-1} with 532 nm laser excitation), characteristic of metallic nanoparticles, its position being consistent with gold, and the detection of elements used in gold nanoparticle preparation allow us to attribute the coloring of pink and carnation areas in several figurines to gold (Table 3).

4.4. Evolution over Time

Given the high variability of compositions, classification based solely on composition is challenging. Only elements associated with cobalt (Table 3) appear to show a trend over time: 17th century cobalt is mainly arsenic-rich, while 18th century compositions are more variable, and cobalt again becomes especially arsenic-rich in figurines from the early 19th century.

5. Conclusions

This first comprehensive study of spun glass figurines demonstrates that these sculptures, like early watches decorated with painted enamels on gold [82–86], reflect both aesthetic sophistication and technical virtuosity in 17th century French fire arts. The variability of glass compositions within the same object distinguishes spun glass figurines from other glass productions. The production process, which involves manipulating a supply of glass in the molten state in a flame, requires adjusting the color and composition of the melt through the addition of several glass rods. As in enameling, it is likely that the last materials added are the most fusible and contain a high amount of lead as in contemporary glazes [87–89] and likely some boron (not detectable by XRF). Consequently, within a single object, glasses of different colors used successively may have distinct compositions. This study also confirms the effectiveness of non-invasive, on-site coupled Raman-pXRF analysis when a semi-quantitative approach is employed. Comparisons of diagrams and dendrograms based on impurities or elements associated with specific ingredients are effective in differentiating the raw materials used.

The analysis confirms the predominant use of $Ca_2Sb_2O_7$ for opacification, occasionally cassiterite (SnO_2: OAP 777, OAP 784 and NOA 969.2.4.3), lead/calcium/potassium arsenate (OAP 255), and even calcium phosphate (OAP 770). The use of cassiterite opacification appears to be more associated with production in Orléans than in Nevers, although more objects from different places would need to be analyzed to confirm this proposition. NOA 2006.0.64 is heavily restored (TiO_2 opacification).

Although historical texts report that the creation of spun glass figurines originated in Venetian workshops, and that the production of glass figurines (without iron frames) continues, to our knowledge no comprehensive analytical study exists for Venetian figurines contemporary with the Nevers collection. Comparative studies would therefore be of interest.

A comparison between a reasoned approach, based on geologically/geochemically characteristic elements of silica, fluxes, and elements diagnostic of different cobalt-rich mineral deposits, and the 'blind' algorithmic approach of chemometric tools such as PCA and Euclidean hierarchical classification shows that these methods are not strictly essential.

Supplementary Materials: The following supporting information can be downloaded at https://www.mdpi.com/article/10.3390/heritage9060230/s1, Table S1: X-ray peak areas of spun glass. Figure S1: X-ray and Raman spectra.

Author Contributions: Conceptualization, P.C.; methodology, P.C. and G.S.-F.; investigation, P.C.; resources, M.-L.C.; data curation, P.C. and G.S.-F.; writing—original draft preparation, P.C. and G.S.-F.; writing—review and editing, P.C., G.S.-F. and M.-L.C.; visualization, P.C. and G.S.-F.; funding acquisition, P.C. All authors have read and agreed to the published version of the manuscript.

Funding: This research was partly funded by Agence Nationale de la Recherche ANR EnamelFC project—19-CE27–0019-02. The APC was funded by P.C.

Data Availability Statement: All data in the paper and Supplementary Materials.

Acknowledgments: Bing Zhao (CRCAO, Collège de France-CNRS, Paris) and Jean Querzola (independent historian) are acknowledged for their help in the preparation of the measurement campaign. All the staff of the Nevers Museum are acknowledged for their help during the measurement week.

Conflicts of Interest: The authors declare no conflicts of interest.

References

1. Cabart, H. *La Verrerie Archéologique: Dieulouard et l'Est de la France Aux XVIe Siècle*; Editions de l'Université de Lorraine: Nancy, France, 2011. [CrossRef]
2. Lanmon, D.P.; Whitehouse, D.B. *Glass in The Robert Lehman Collection: XI Glass*; The Metropolitan Museum of Art in Association with Princeton University Press: New York, NY, USA; Princeton, NJ, USA, 1993; pp. 231–233.
3. Perret-Gentil, E. Conservation-Restauration d'un Diorama en Verre Filé et Perles Présentant Une vue de la Place Saint-Marc de Venise un Jour de Carnaval. Master's Dissertation, Haute Ecole Arc Conservation-Restauration, Neuchâtel, Switzerland, 2020. Available online: https://folia.unifr.ch/global/documents/313434 (accessed on 10 March 2026).
4. Barrelet, J. Le verre filé à propos d'une crèche. *Cah. Céramique Verre Arts Feu* **1940**, *20*, 12–20.
5. Bellanger, J. Figurines de verre et d'émaux de Nevers. *Revue Verre* **2004**, *10*, 49–55.
6. Rossi-Wilcox, S.M.; Reiling, H.; Bisaga, P. The Blashkas' Lampworkin tables. *J. Glass Stud.* **2003**, *45*, 167–176.
7. Davison, S. A review of adhesives and consolidants used on glass antiquities. *Stud. Conserv.* **1984**, *29*, 191–194. [CrossRef]
8. Colomban, P.; Kırmızı, B. Non-invasive on-site Raman study of polychrome and white enamelled glass artefacts in imitation of porcelain assigned to Bernard Perrot and his followers. *J. Raman Spectrosc.* **2020**, *51*, 133–146. [CrossRef]
9. Lahlil, S. Redécouverte des Procédés D'opacification des Verres à L'antimoine à Travers L'Histoire. Etude des Antimoniates de Calcium. Ph.D. Dissertation, Université Pierre et Marie Curie-Paris VI, Paris, France, 2008.
10. Lahlil, S.; Cotte, M.; Biron, I.; Szlachetko, J.; Menguy, N.; Susini, J. Synthesizing lead antimonate in ancient and modern opaque glass. *J. Anal. At. Spectrom.* **2011**, *26*, 1040–1050. [CrossRef]
11. Lahlil, S.; Biron, I.; Galoisy, L.; Morin, G. Rediscovering ancient glass technologies through the examination of opacifier crystals. *Appl. Phys. A* **2008**, *92*, 109–116. [CrossRef]
12. Colomban, P.; Gironda, M.; Simsek Franci, G.; d'Abrigeon, P. Distinguishing genuine imperial Qing dynasty porcelain from ancient replicas by on-site non-invasive XRF and Raman spectroscopy. *Materials* **2022**, *15*, 5747. [CrossRef]
13. Colomban, P.; Simsek Franci, G.; Gerken, M.; Gironda, M.; Mesqui, V. Non-Invasive On-Site XRF and Raman Classification and Dating of Ancient Ceramics: Application to 18th and 19th Century Meissen Porcelain (Saxony) and Comparison with Chinese Porcelain. *Ceramics* **2023**, *6*, 2178–2212. [CrossRef]
14. Colomban, P.; Simsek Franci, G.; Burlot, J.; Gallet, X.; Zhao, B.; Clais, J.B. Non-Invasive on-Site pXRF Analysis of Coloring Agents, Marks and Enamels of Qing Imperial and Non-Imperial Porcelain. *Ceramics* **2023**, *6*, 447–474. [CrossRef]
15. Available On-Line Bruker. Available online: https://xrfcheck.bruker.com/InfoDepth (accessed on 9 March 2026).
16. Guerrero Rivero, S.A.; da Silva Gondim, L.; Torres, J.B.; Teixeira, A.; Tavares, N.P.; Monteiro, J.; Iñañez, J. Early Modern Creole and Iberian Ceramics in Cape Verde: Non-Destructive pXRF Analysis of 16th–18th Century Pottery from Santiago Island. *Ceramics* **2026**, *9*, 13. [CrossRef]

17. Occari, V.; Fenwick, C.; Möller, H.; Quinn, P.S.; Freestone, I.C.; Sacco, V.; von Rummel, P.; Chaouali, M. Kairouan and the medieval ceramic industry in Tunisia: New data from compositional analysis of glazed and unglazed wares from the sites of Bulla Regia and Chimtou. *J. Archaeol. Sci. Rep.* **2025**, *66*, 105245. [CrossRef]
18. Aitchison, J. *The Statistical Analysis of Compositional Data*; Chapman and Hall: London, UK, 1986.
19. Chen, G.; Cheng, Z.; Li, G.; Fang, J.; Huang, G.; Bao, C.; Wang, Z.; Zhan, C. Provenance of ancient porcelains from the Xisha (Paracels) Islands: Integrating chemical, microstructural, and magnetic techniques. *J. Eur. Ceram. Soc.* **2026**, *46*, 1179855. [CrossRef]
20. Mangone, A.; Giannossa, L.C.; Biscotti, C.; Taccogna, C.; Laganara, C. Innovative technological strategies in the surface treatment of Medieval glazed ceramics. *npj Herit. Sci.* **2026**. [CrossRef]
21. Lee, Y.J.; Kim, G.-W.; Jeong, C.W.; Kim, H.T.; Choi, M.J.; Park, S.B.; Lee, T.-J.; Kim, H.J. Raman Spectroscopy and One-Dimensional Convolutional Neural Networks for the Forensic Identification of Red Stamp Inks in Questioned Documents. *J. Raman Spectrosc.* **2026**, *57*, 80–93. [CrossRef]
22. Hwang, S.-W.; Park, G.; Kim, J.; Kang, K.-H.; Lee, W.-H. One-Dimensional Convolutional Neural Networks with Infrared Spectroscopy for Classifying the Origin of Printing Paper. *BioResources* **2024**, *19*, 1633–1651. [CrossRef]
23. Lee, Y.J.; Kweon, S.W.; Jeong, C.W.; Kim, H.J. Evaluating the Performance of Machine Learning and Variable Selection Methods to Identify Document Paper Using Infrared Spectral Data. *Spectrochim. Acta. Part A Mol. Biomol. Spectrosc.* **2025**, *327*, 125299. [CrossRef]
24. Lee, Y.J.; Won, S.Y.; Park, S.B.; Kim, H.-J. Chemometric Approaches for Discriminating Manufacturers of Korean Handmade Paper Using Infrared Spectroscopy. *Herit. Sci.* **2024**, *12*, 373. [CrossRef]
25. Lee, Y.-J.; Lee, T.-J.; Kim, H.J. Classification Analysis of Copy Papers Using Infrared Spectroscopy and Machine Learning Modeling. *BioResources* **2023**, *19*, 160–182. [CrossRef]
26. Lee, Y.J.; Jeong, C.W.; Kim, H.T.; Lee, T.J.; Kim, H.J. Raman Spectroscopy and Machine Learning for Forensic Document Examination. *Analyst* **2025**, *150*, 1785–1794. [CrossRef]
27. Altman, D.G.; Bland, J.M. Diagnostic Tests. 1: Sensitivity and Specificity. *BMJ* **1994**, *308*, 1552. [CrossRef]
28. Wang, T.; He, Z.; Xia, S.; Sciau, P.; Shao, A.; Ren, Z.; Wang, F.; Zhu, J.; Wang, Y.; Li, Q.; et al. Micro-Raman Study of Chinese Iron-Based Brown Wares Produced During Song Dynasty (960–1279 CE): Probing Crystals in the Glazes. *Heritage* **2025**, *8*, 480. [CrossRef]
29. Tankova, V.; Atanassova, V.; Mihailov, V.; Pirovska, A. Identification of Mineral Pigments on Red- and Dark-Decorated Prehistoric Pottery from Bulgaria. *Minerals* **2025**, *15*, 877. [CrossRef]
30. Colomban, P.; Tournié, A.; Bellot-Gurlet, L. Raman identification of glassy silicates used in ceramics, glass and jewellery: A tentative differentiation guide. *J. Raman Spectrosc.* **2006**, *37*, 841–852. [CrossRef]
31. Ricciardi, P.; Colomban, P.; Tournié, A.; Macchiarola, M.; Ayed, N. A non-invasive study of Roman Age mosaic glass tesserae by means of Raman spectroscopy. *J. Archaeol. Sci.* **2009**, *36*, 2551–2559. [CrossRef]
32. Manoun, B.; Azdouz, M.; Azrour, M.; Essehli, R.; Benmokhtar, S.; El Ammari, L.; Ezzahi, A.; Ider, A.; Lazor, P. Synthesis, Rietveld refinements and Raman spectroscopic studies of tricationic lacunar apatites $Na_{1-x}K_xPb_4(AsO_4)_3$ ($0 \leq x \leq 1$). *J. Mol. Struct.* **2011**, *986*, 1–9. [CrossRef]
33. Van Pevenage, J.; Lauwers, D.; Herremans, D.; Verhaeven, E.; Vekemans, B.; De Clercq, W.; Vincze, L.; Moens, L.; Vandenabeele, P. A combined spectroscopic study on Chinese porcelain containing ruan-cai colours. *Anal. Methods* **2014**, *6*, 387–394. [CrossRef]
34. Mazza, T.; Barborini, E.; Piseri, P.; Milani, P.; Cattaneo, D.; Li Bassi, A.; Bottani, C.E.; Ducati, C. Raman spectroscopy characterization of TiO_2 rutile nanocrystals. *Phys. Rev. B* **2007**, *75*, 045416. [CrossRef]
35. Lawrence Berkeley National Laboratory, XRF Tables. Available online: https://xdb.lbl.gov/Section1/Table_1-2.pdf (accessed on 16 March 2026).
36. Kissin, S.A. Five-element (Ni-Co-As-Ag-Bi) veins. *Geosci. Can.* **1992**, *19*, 113–124. Available online: https://journals.lib.unb.ca/index.php/gc/article/view/3768/4282 (accessed on 20 March 2026).
37. Colomban, P.; Kirmizi, B.; Simsek Franci, G. Cobalt and associated impurities in blue (and green) glass, glaze and enamel: Relationships between raw materials, processing, composition, phases and international trade. *Minerals* **2021**, *11*, 633. [CrossRef]
38. Molera, J.; Climent-Font, A.; Garcia, G.; Pradell, T.; Vallcorba, O.; Zucchiatti, A. Experimental study of historical processing of cobalt arsenide ore for colouring glazes (15–16th century Europe). *J. Archaeol. Sci. Rep.* **2021**, *36*, 102797. [CrossRef]
39. Čermáková, Z.; Hradil, D.; Míková, J.; Hradilová, J.; Rohanová, D. Co-glass and blue pigment smalt production at the turn of the 15th/16th centuries: LA-ICP-MS study. *Archaeol. Anthropol. Sci.* **2026**, *18*, 68. [CrossRef]
40. Banda, W.; Morgan, N.; Eksteen, J.J. The role of slag modifiers on the selective recovery of cobalt and copper from waste smelter slag. *Miner. Engn.* **2002**, *15*, 899–907. [CrossRef]
41. Berrie, B.H. Mining for color: New blues, yellows, and translucent paint. *Early Sci. Med.* **2015**, *20*, 308–334. [CrossRef]
42. Gratuze, B.; Soulier, I.; Barrandon, J.N.; Foy, D. De l'origine du cobalt dans les verres. *Rev. D'Archéométrie* **1992**, *16*, 97–108.

43. Gratuze, B.; Soulier, I.; Blet, M.; Vallauri, L. De l'origine du cobalt: Du verre à la céramique. *Rev. D'Archéométrie* **1996**, *20*, 77–94. [CrossRef]
44. Sakellariou, K.; Miliani, C.; Morresi, A.; Ombelli, M. Spectroscopic investigation of yellow majolica glazes. *J. Raman Spectrosc.* **2004**, *35*, 61–67. [CrossRef]
45. Sandalinas, C.; Ruiz-Moreno, S.; Lopez-Gil, A.; Miralles, J. Experimental confirmation by Raman spectroscopy of a Pb-Sn-Sb triple oxide yellow pigment in sixteenth-century Italian pottery. *J. Raman Spectrosc.* **2006**, *37*, 1146–1153. [CrossRef]
46. Rosi, F.; Manuali, V.; Miliani, C.; Brunetti, B.G.; Sgamellotti, A.; Grygar, T.; Hradil, D. Raman scattering features of lead pyroantimonate compounds. Part I: XRD and Raman characterization of $Pb_2Sb_2O_7$ doped with tin and zinc. *J. Raman Spectrosc.* **2009**, *40*, 107–111. [CrossRef]
47. Pelosi, C.; Agresti, G.; Santamaria, U.; Mattei, E. Artificial yellow pigments: Production and characterization through spectroscopic methods of analysis. *e-Preserv. Sci.* **2010**, *7*, 108–115. Available online: http://www.morana-rtd.com/e-preservationscience/2010/Pelosi-10-05-2010.pdf (accessed on 25 May 2023).
48. Pereira, M.; de Lacerda-Aroso, T.; Gomes, M.J.M.; Mata, A.; Alves, L.V.; Colomban, P. Ancient Portuguese Ceramic Wall Tiles (« Ajulejos »): Characterization of the Glaze and Ceramic Pigments. *J. Nano Res.* **2009**, *8*, 79–88. [CrossRef]
49. Burlot, J.; Vangu, D.; Bellot-Gurlet, L.; Colomban, P. Raman identification of pigments and opacifiers. Interest and limitation of multivariate analysis by comparison with solid state spectroscopical approach. I. Lead-tin and Naples yellow. *J. Raman Spectrosc.* **2024**, *55*, 161–183. [CrossRef]
50. Colomban, P.; Tang, H.; Simsek-Franci, G. Non-Invasive Study of Gold Nanoparticles in Famille rose and Ruby-Back Qing Porcelain by Luminescence, Low-Wavenumber Raman Scattering and pXRF. *Appl. Sci.* **2025**, *15*, 12265. [CrossRef]
51. Colomban, P. The use of metal nanoparticles to produce yellow, red and iridescent colour, from bronze age to present times in lustre pottery and glass: Solid state chemistry, spectroscopy and nanostructure. *J. Nano Res.* **2009**, *8*, 109–132. Available online: https://www.scientific.net/jnanor.8.109 (accessed on 20 March 2026).
52. Brun, N.; Mazerolles, L.; Pernot, M. Microstructure of opaque red glass containing copper. *J. Mater. Sci. Lett.* **1991**, *10*, 1418–1420. [CrossRef]
53. Sciau, P.; Noé, L.; Colomban, P. Metal nanoparticles in contemporary potters' master pieces: Lustre and red "pigeon blood" potteries as models to understand the ancient pottery. *Ceram. Int.* **2016**, *42*, 15349–15357. [CrossRef]
54. Geyssant, J. (Ed.) *Bernard Perrot (1640–1709), Secrets and Masterpieces of the Royal Glassworks of Orléans, Catalogue*; Musée des Beaux-Arts d'Orléans—SOMOGY Editions d'Arts: Paris, France, 2013. (In French)
55. Chen, T.-H. Aventurine glass in Western and Eastern History: Occurrence, fabrication and artistry. In Proceedings of the International Conference on Glass in Archaeology and History: Cultural, Economic and Artistic Exchanges, Taipei, Taiwan, 27 March 2018. (Abstract n°7).
56. Cormier, L. Synthetic (Goldstone) and Natural Aventurine—A Review. *Glass Eur.* **2025**, *3*, 165–181. [CrossRef]
57. Zecchin, P. La pasta venturina, vetro speciale muranese. *J. Glass Stud.* **2005**, *47*, 93–106.
58. Yap, C.T. EDXRF studies on the variation in elemental concentrations of ceramic glazes. *X-Ray Spectrom.* **1989**, *18*, 31–34. [CrossRef]
59. Leung, P.L.; Luo, H. A study of provenance and dating of ancient Chinese porcelain by x-ray fluorescence spectrometry. *X-Ray Spectrom.* **2000**, *29*, 34–38. [CrossRef]
60. Bezur, A.; Casadio, F. The analysis of porcelain using handheld and portable X-ray fluorescence spectrometers. In *Handheld XRF for Art and Archaeology*; Leuven University Press: Leuven, Belgium, 2013; pp. 249–312.
61. Colomban, P.; Simsek Franci, G.; Gallet, X. Non-Invasive Mobile Raman and pXRF Analysis of Armorial Porcelain with the Coat of Arms of Louis XV and Others Enamelled in Canton: Analytical Criteria for Authentication. *Heritage* **2024**, *7*, 4881–4913. [CrossRef]
62. Colomban, P.; Franci, G.S.; Gerken, M.; Gironda, M.; Mesqui, V. Chemical and vibrational criteria for identifying early Sèvres factory porcelain productions. *Ceramics* **2024**, *7*, 1905–1927. [CrossRef]
63. Simsek, G.; Colomban, P.; Wong, S.; Zhao, B.; Rougeulle, A.; Liem, N.Q. Toward a fast non-destructive identification of pottery: The sourcing of 14th–16th century Vietnamese and Chinese ceramic shards. *J. Cult. Herit.* **2015**, *16*, 159–172. [CrossRef]
64. Gower, J.C. A comparison of some methods of cluster analysis. *Biometrics* **1967**, *23*, 623–637. [CrossRef]
65. Sparks, D.N. Euclidean cluster analysis. *JR Stat. Soc. Ser. C Appl. Stat.* **1973**, *22*, 126–130. [CrossRef]
66. Picon, M. Le traitement des données d'analyse, Datation-caractérisation des céramiques anciennes. *Pact* **1984**, *10*, 379–399.
67. Picon, M. L'analyse chimique des céramiques: Bilan et perspectives. In *Archeometria Della Ceramica, Problemi di Metodo: Atti 8^e Simposio Internatzionale Della Ceramica, Rimini 1992*; Bianchi, S.S., Ed.; Centro Ceramico: Bologna, Italy, 1993; pp. 3–26.
68. Mommsen, H.; Kreuser, A.; Weber, J. A method for grouping pottery by chemical composition. *Archaeometry* **1988**, *30*, 47–57. [CrossRef]
69. Waksman, Y. Provenance Studies. In *The Oxford Handbook of Archaeological Ceramic Analysis*; Oxford University Press: Oxford, UK, 2016; pp. 3341–3360.

70. Maritan, L.; Holakooei, P.; Mazzoli, C. Cluster analysis of XRPD data in ancient ceramics: What for? *Appl. Clay Sci.* **2015**, *114*, 540–549. [CrossRef]
71. Maggetti, M.; Rosen, J.; Serneels, V. The Origin of 18th–19th Century Tin-Glazed Pottery from Lorraine, France. *Archaeometry* **2015**, *57*, 426–452. [CrossRef]
72. Qi, F.; Wei, G.; Qin, J.; Gan, H. A comparative study on pottery raw materials in two late neolithic sites in Northern Jiangsu, China. *Eur. Phys. J. Plus* **2025**, *140*, 687. [CrossRef]
73. Bourdin, V.; Delbey, T.; Rasmussen, K.L.; Charlier, P. Do you dig your grave with your teeth? Potential interest of the elementary analysis of ancient ceramics regarding public health (Pre-Columbian era, Ecuador). *Ethics Med. Public Health* **2022**, *23*, 100794. [CrossRef]
74. Burlot, J.; Waksman, S.Y. Provenances and production techniques of the so-called 'Port Saint Symeon ware' (13th–early 14th centuries ce) from Kinet Höyük (Cilicia, Turkey): Witnessing interactions in the medieval north-eastern Mediterranean. *Archaeometry* **2022**, *64*, 611–631. [CrossRef]
75. Rahman, M.S.; Metselaar, H.S.C. XRF data-based statistical clustering of ancient ceramic artifacts and analysing provenance with thermo-mineralogical analysis. *Spectrochim. Acta Part B At. Spectrosc.* **2025**, *224*, 107090. [CrossRef]
76. Badawy, W.M.; Dmitriev, A.Y.; Koval, V.Y.; Smirnova, V.S.; Chepurchenko, O.E.; Lobachev, V.V.; Belova, M.O.; Galushko, A.M. Formation of reference groups for archaeological pottery using neutron activation and multivariate statistical analyses. *Archaeometry* **2022**, *64*, 1377–1393. [CrossRef]
77. Akyuz, S.; Celik, S.; Kurap, G.; Ozel, A.E.; Basaran, S. Investigations of black and red figure pottery shards and local clay, excavated at Ainos (Enez-Turkey), by multiple analytical techniques. *Vib. Spectrosc.* **2023**, *129*, 103613. [CrossRef]
78. Burlot, J.; Colomban, P.; Bellot-Gurlet, L.; Lemasson, Q.; Pichon, L. Non-invasive analyze of boron and lithium in 18th century Chinese porcelain enamel and glaze: A PIXE/PIGE study. *J. Eur. Cer. Soc.* **2024**, *44*, 116746. [CrossRef]
79. Swan, C.M.; Rehren, T.; Dussubieux, L.; Eger, A.A. High-boron and high-alumina middle Byzantine (10th–12th century CE) glass bracelets: A western Anatolian glass industry. *Archaeometry* **2018**, *60*, 207–232. [CrossRef]
80. Maestro-Guijarro, L.; Sedano, M.; Schibille, N.; Pradell, T.; Castillejo, M.; Oujja, M.; Palomar, T. Determination of Boron Content in Surface Paintings From Historical Stained-Glass Windows. *Chem.-Methods* **2025**, *5*, e202400057. [CrossRef]
81. Biron, I.; Gratuze, B.; Pistre, S.; Lehuede, P. *Etude En Laboratoires D'Objets en Verre Attribués à Bernard Perrot*; Bulletin De L'association Française Pour L'archéologie Du Verre: Paris, France, 2011; pp. 19–26. Available online: https://afaverre.fr/Afaverre/wp-content/uploads/2025/01/04_Isabelle-Biron-2011_v2.pdf (accessed on 20 March 2026).
82. Colomban, P.; Kırmızı, B.; Gougeon, C.; Gironda, M.; Cardinal, C. Pigments and glassy matrix of the 17th–18th century enamelled French watches: A non-invasive on-site Raman and pXRF study. *J. Cult. Herit.* **2020**, *44*, 1–14. [CrossRef]
83. Cardinal, C. *La Collection des Montres et Horloges de Table du Musée du Louvre*; Tome 1 (1984); Tome 2 (2000); RMN: Paris, France, 2000.
84. Cardinal, C. *La Montre des Origines au XIXe Siècle*; Office du Livre: Fribourg, Switzerland, 1985.
85. Cardinal, C. L'horloge, un objet emblématique de la Renaissance. In *Trésors D'horlogerie, Le Temps et Sa Mesure Du Moyen-Age À La Renaissance*; Editions RMG/Palais des Papes: Avignon, France, 1998.
86. Vincent, C. Some seventeenth-century French painted enamel watchcases. *Metrop. Mus. J.* **2002**, *37*, 89–106. [CrossRef]
87. Bouquillon, A.; Castaing, J.; Barbe, F.; Crepin-Leblond, T.; Tilliard, L.; Paine, S.R.; Christman, B.; Heuer, A.H. French decorative ceramics mass-produced during and after the 17th century: Chemical analyses of the glazes. *Archaeometry* **2018**, *60*, 946–965. [CrossRef]
88. Pradell, T.; Molera, J. Ceramic technology. How to characterise ceramic glazes. *Archaeol. Anthropol. Sci.* **2020**, *12*, 189. [CrossRef]
89. Bouquillon, A.; Castaing, J.; Barbe, F.; Paine, S.R.; Christman, B.; Crépin-Leblond, T.; Heuer, A.H. Lead-Glazed Rustiques Figulines (Rustic Ceramics) of Bernard Palissy (1510–90) and his Followers. *Archaeometry* **2017**, *59*, 69–83. [CrossRef]

Disclaimer/Publisher's Note: The statements, opinions and data contained in all publications are solely those of the individual author(s) and contributor(s) and not of MDPI and/or the editor(s). MDPI and/or the editor(s) disclaim responsibility for any injury to people or property resulting from any ideas, methods, instructions or products referred to in the content.